The Numerical Simulation of Nonsupercell Tornadogenesis. Part II: Evolution of a Family of Tornadoes along a Weak Outflow Boundary

BRUCE D. LEE* AND ROBERT B. WILHELMSON

Department of Atmospheric Sciences and National Center for Supercomputing Applications, University of Illinois, Urbana, Illinois

(Manuscript received 6 November 1996, in final form 31 March 1997)

ABSTRACT

Nonsupercell tornadogenesis along a weak outflow boundary has been simulated using a three-dimensional moist convective cloud model. Thermodynamic conditions similar to those observed for nonsupercell tornado (NST) events of the High Plains were utilized in the model initialization. As the ensemble system of storm, outflow boundary, and leading edge vortices evolve, six distinct life cycle stages for the development and decay of NSTs are documented that span a period of about 35 min. Consistent with the results of Part I of this numerical study, vortex sheet dynamics exert considerable control over the outflow leading edge. The progression of pretornadic life cycle stages serves to concentrate vertical vorticity effectively along the outflow boundary in discrete misocyclone circulations aligned in a 3-km wavelength pattern. The organization of larger-scale misocyclones and ultimate intensification to initial tornadic intensity occurs coincident with the rapid development of deep convection overhead. The strongest members of a family of NSTs that develop in the model maintain ground-relative surface wind speeds of greater than 30 m s^{-1} for approximately 11 min within which wind speeds meet F1 severity criteria for 6 min. The mature vortices reach the midlevels of the moist convection and display deep, rotationally induced axial downdrafts. The rapid transition to a predominant downdraft character for the storm complex and to an outflow dominated subcloud air mass heralds the onset of NST dissipation. The NST evolution simulated here compares very favorably to observational NST studies.

The misocyclones are shown to provide an asymmetric pattern of convective forcing along the outflow boundary, which supports the formation of deep moist convection directly over them. Vertical vorticity in the boundary layer misocyclones is redistributed upward into the midlevels of the moist convection (~6 km) by developing deep updrafts. The mature vortices are maintained by vertical vorticity transported from a vortex sheet located along the outflow boundary and by vertical vorticity produced from the tilting of horizontal vorticity in the inflow region southeast of the NSTs. Low-level vortex stretching is the dominant vorticity tendency term as the vortices intensify to and maintain tornadic strength. No significant vertical tilting of baroclinically generated horizontal vorticity was indicated even after convective downdraft-associated new outflow pools formed in the environment surrounding the misocyclones. These new outflow pools play a major role in NST intensification by increasing convergence and resultant vortex stretching along the periphery of the tornadic circulations. A comparative simulation with rain production turned off, which precluded the possibility of new outflow development, revealed that NST intensity was roughly 25% greater in the baseline simulation. In an additional comparative simulation where no moist convection was allowed to develop, the resultant misocyclones markedly lacked the coherent organization and intensity of the misocyclones and NSTs of the baseline simulation and no NST-strength vortices developed. A six-stage ''refined'' model of NST development and decay is presented.

1. Introduction

In Part I of this series of articles on the simulation of nonsupercell tornadogenesis (NSTG), misocyclone initiation and evolution were investigated along outflow boundaries possessing significant across-front horizontal shear with a dry, nonhydrostatic, three-dimensional numerical model (Lee and Wilhelmson 1997, hereafter LW97). Misocyclone circulations, which by definition (Fujita 1981) have diameters less than 4 km, are the parent circulations of nonsupercell tornadoes. The sensitivity of misocyclone development to variations in environment vertical shear, across-front horizontal shear, and ambient stability were presented in addition to an examination of the influence surface friction has on misocyclone evolution.

In this paper, NSTG is simulated in a moist environment with a three-dimensional convective cloud model. Tornadogenesis is examined along a weak outflow boundary with thermodynamic conditions similar to that often associated with observed nonsupercell tornado (NST) events of the High Plains. The overarching objective of this phase of the numerical investigation in-

*Current affiliation: Department of Earth Sciences, University of Northern Colorado, Greeley, Colorado.

Corresponding author address: Dr. Bruce D. Lee, Department of Earth Sciences, University of Northern Colorado, 501 20th Street, Greeley, CO 80639.
E-mail: bdlee@bentley.unco.edu

volves the basic understanding of the life cycle stages of NSTs and their parent misocyclones in the presence and influence of deep moist convection. The process by which lower-tropospheric misocyclones influence the character of the deep convection and how this deep convection ultimately affects the intensification of the misocyclone is not well understood. Specifically, we wish to understand how storm processes such as the creation of new outflow regions influence the NST. Two additional motivations for this research include 1) the confirmation of various features associated with NSTs that have only been rarely observed and 2) the verification and refinement of the observational model of NSTG.

The reader is referred to LW97 for a review of observational, theoretical, and modeling studies relevant to NSTs and NSTG. A short summary is included here on NSTs and the conceptual model of NSTG that has resulted from observational studies. The terms ''nonsupercell tornado'' as given by Wakimoto and Wilson (1989, hereafter WW89) or ''nonmesocyclone tornado'' as given by Brady and Szoke (1989, hereafter BS89) have been used to describe tornadoes associated with storms not displaying the prominent pretornadic midlevel rotation found in supercell storms. Bluestein (1985) coined the name ''landspout'' to describe certain NSTs that have a similar visual appearance to waterspouts. The current ''observational model'' for NSTG became established as more NST cases were analyzed, most of which occurred near the National Center for Atmospheric Research's observational network in northeast Colorado. Studies by Wilson (1986), WW89, and BS89 built the foundation for this model of NSTG. Common attributes of NST environments include 1) the presence of a mesoscale surface boundary possessing significant across-front horizontal shear (i.e., vertical vorticity), 2) misocyclones circulations along the boundary, 3) rapidly growing cumulus congestus or young cumulonimbus along the boundary, and 4) only weak mid- and upper-tropospheric winds. If a fortunate juxtaposition of moist convective updraft and misocyclone occurs, the vortex may be stretched to tornadic intensity (see WW89's Fig. 20). The results from a comprehensive observational dual-Doppler study by Roberts and Wilson (1995, hereafter RW95) of the 15 June 1988 Denver multiple NST event have closely matched and added detail to this observational model. In contrast to this model, Wilczak et al. (1992) found that the vertical tilting of baroclinically generated horizontal vorticity played an important role in tornado formation, based on a multiple-Doppler study of a Colorado NST.

The model and experimental design for these simulations are presented in section 2, followed in section 3 by results detailing the development and decay of a ''family'' of NSTs and associated deep moist convection that developed in this simulation. For clarity, the expression family as used here defines several simultaneously occurring tornadoes, as contrasted with certain supercell family tornado events associated with cyclic tornado production occurring over several-hour periods. In this study, a vortex is arbitrarily defined as an NST when its ground relative winds exceed 30 m s^{-1} (i.e., high F0 velocity criteria; see Fujita 1981). In section 4 an analysis of the life cycle of one particular tornado is presented, which includes an examination of vorticity redistribution, maintenance, and intensification. Section 5 features the impact of new outflow from storms initiating along the outflow leading edge on NST intensification and examines the effect of overhead deep moist convection on the boundary layer misocyclones. A ''refined'' model of NSTG is presented in section 6 that incorporates the results from observational studies, LW97, and this numerical investigation.

2. Model description and experimental design

a. The model

A three-dimensional, nonhydrostatic, quasi-compressible, finite difference convective cloud model called MSTFLOW is employed to simulate NSTG along a weak outflow boundary. This model is a hybrid spinoff of the Klemp and Wilhelmson (1978) cloud model and the COMMAS model (Wicker and Wilhelmson 1995) and was designed to utilize the massively parallel Connection Machine (CM-5) at the National Center for Supercomputing Applications. The high speed and large memory CM-5 proved to be an ideal platform on which to run the high-resolution simulations necessary for this investigation (see the appendix in LW97 for code performance information on this platform).

The MSTFLOW model is described in the appendix; consequently, only a broad summary is presented here. The Coriolis force is neglected in these experiments, in keeping with the high Rossby number nature of the flows being simulated. MSTFLOW utilizes a Kessler cloud microphysics formulation similar to that used in Klemp and Wilhelmson (1978) and Durran and Klemp (1983). A diagnostic subgrid-scale mixing parameterization is employed (Smagorinsky 1963; Lilly 1962; Clark 1979). A bulk aerodynamic surface friction parameterization identical to that employed by Wilhelmson and Chen (1982) is included in the model to represent a ''semi-slip'' condition at the model surface. Within this formulation, a drag coefficient (C_D) of 0.002 was used. A geometric mapping (Walko 1988) is used to stretch the grid vertically. The model has rigid upper and lower boundaries (i.e., $w = 0$). To prevent artificial reflection of vertically propagating gravity waves off the upper domain lid, a Rayleigh sponge layer is applied in the model above 11 km. The effective viscosity of this layer is gradually increased such that vertically propagating waves have zero amplitude by the time they reach the model top. The lateral boundaries were open in the west–east direction and cyclic in the north–south direction. The open lateral boundary conditions used by

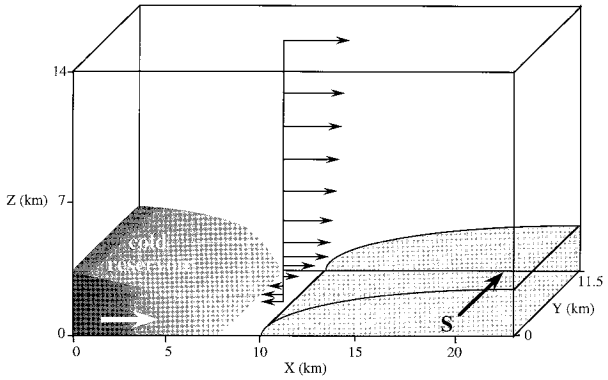

FIG. 1. Initial configuration of the model domain that contains a cold reservoir (dark gray transition shading), a region of southerlies (light gray shading with ''S'' designator), and the vertical profile of the west–east winds present over the entire domain (see text for specific details).

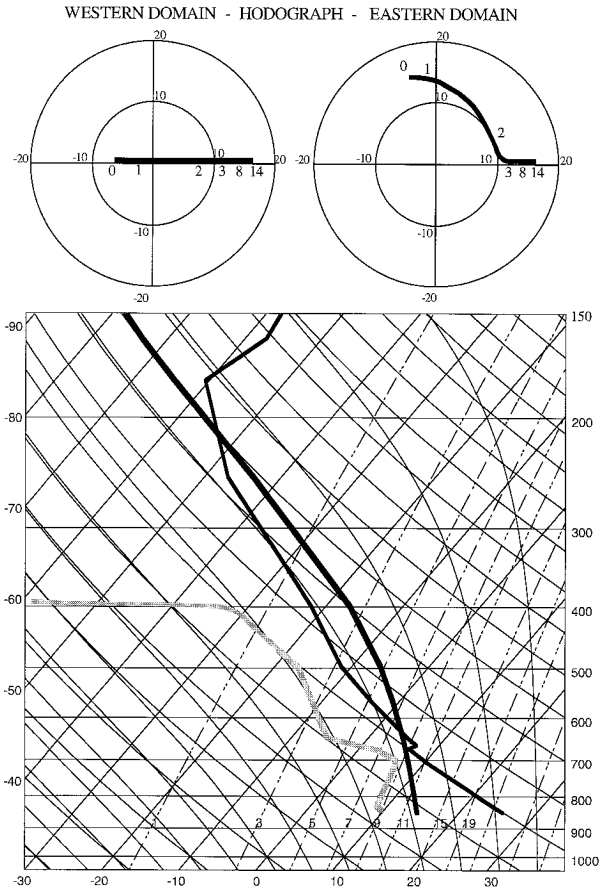

FIG. 2. Hodographs representing the initial vertical structure of the horizontal winds present in the western and eastern portions of the model domain and a skew-*T* diagram of the thermodynamic conditions outside of the cold reservoir region.

Klemp and Wilhelmson (1978) are adopted and allow internally generated gravity waves to pass smoothly out of the domain with a minimum of reflection. The cyclic north–south condition is both computationally efficient and effective for studying the time evolution of instabilities that have periodic characteristics in the north–south direction.

These simulations employed a 384 × 192 × 50 point grid with 60-m horizontal grid spacing and a stretched vertical grid with spacing ranging from 40 m at the surface to 700 m near the top of the domain. This stretched vertical grid configuration places 23 grid points in the dynamically critical surface to 2-km layer. The model domain size (23 km × 11.5 km × 14 km) shown in Fig. 1 was chosen such that NSTG and the concurrently evolving storms at the outflow leading edge could reach some semblance of maturity while remaining well within the domain interior (with respect to the east–west domain boundaries). The domain was allowed to move at the speed of the propagating density current initially and then tuned to the propagation speed of the vortex and storm system. The north–south domain width was selected such that this dimension would be much larger than the wavelength of the evolving misocyclones along the leading edge (~1.3–3 km), thus ensuring that the misocyclone wavelength is being driven by the dynamics of the problem and not the north–south dimension of the domain.

b. Initialization

The initial conditions are designed to represent a northeast Colorado NST scenario involving a weak outflow boundary. This weak outflow boundary is created in the model via a quasi ''dam break'' initialization whereby a cold reservoir is allowed to collapse, creating an outflowlike density current in the model domain (Fig. 1) in a manner similar to that employed in Part I (see LW97 for a detailed description of this outflow initialization). The maximum temperature deficit in this reservoir is −2.5 K, a value typical of weak summer outflow boundaries in northeast Colorado (Mahoney 1988). The initial cold reservoir shape is described by an elliptical arc with a horizontal major axis radius of 7 km and a vertical minor axis radius of 3.5 km. The reservoir temperature deficit transitions from a maximum deficit along the western boundary to no deficit using a cosine function of *x*. There is no vertical variation of perturbation potential temperature within the reservoir.

Heterogeneous initial conditions in the model wind field shown in Fig. 1 and on the hodographs of Fig. 2 are utilized such that, as the outflow propagates forward, a region of significant horizontal shear (a vertical vortex sheet) is created at the leading edge. A broad transition region is included at the interior edge of the region of southerly winds that avoids an artificial introduction of a strong vertical vortex sheet into the model. Initial horizontal shear (vertical vorticity) on the western periphery of the region of southerlies in the boundary layer before cold reservoir collapse is 0.005 s^{-1}. The creation of a strong vortex sheet is left to the propagating outflow

boundary and its interaction with the southerly flow, which has a maximum magnitude of 15 m s^{-1} near the surface. The differential velocity of the line parallel wind (across the leading edge) based on observational NST studies ranges from 5 to 30 m s^{-1}; thus our choice of a 15 m s^{-1} maximum southerly wind lies well within this observational range. The model domain wind field contains a vertical shear profile in u such that outflow leading edge and the misocyclones residing there are vertically erect (Rotunno et al. 1988; Xu and Moncrieff 1994; Chen 1995). Trial simulations using strong outflow boundaries (temperature deficits up to -8 K) required unrealistically large vertical shear magnitudes (relative to documented northeast Colorado NST cases) in the ambient environment to produce erect updraft structure at the outflow leading edge. A thermodynamic profile composited from several northeast Colorado NST cases is used (Fig. 2) that features a convective available potential energy (CAPE) of 1060 m^2 s^{-2} and a lifted index of -5. This profile consists of a dry adiabatic boundary layer below a small capping inversion at the 670-mb level. An elevated well-mixed layer exists between 510 and 670 mb. The equilibrium level from surface based parcel ascent lies at the 210-mb level.

To introduce subtle three-dimensionality to the cold pool initial conditions, very small random thermal perturbations were placed into the first eastern kilometer of the cold reservoir. These perturbations were assigned to two gridpoint groupings (120 m) in the y direction and had a height and length of 1 km. In total, 96 thermal perturbations whose magnitude randomly ranged between -0.2 and 0.0 K were laid out along the cold pool leading edge.

A technique delaying the collapse of the cold pool for a 200-s time period at the start of the model integration was utilized to prevent the cold reservoir from shearing apart given the environment of vertical shear in which it initially resided. To accomplish this, the potential temperature field was prevented from updating during this 200-s span, while all other model variables except the moist microphysics variables were allowed to update. As the pressure and vertical velocity fields responded to the cold pool presence, a thermally direct circulation developed at the cold pool leading edge such that upon reaching 200 s, the cold reservoir collapses in a more realistic manner.

c. Parameter studies

To further understand the role that storm processes play in NSTG, two parameter studies were undertaken. The first of these involved the role played by precipitation-generated new outflow from overhead or directly adjacent storms on the intensification and demise of the NST. A simulation designated ''No-Qr'' was conducted in which the rain microphysics processes in MSTFLOW were turned off to prohibit ''new'' outflow development through evaporation and precipitation downloading. The second parameter study involved the role played by the overlying moist convection on the NSTG process. To investigate this, the moist microphysics of MSTFLOW were turned off entirely in a simulation designated ''No-Qc,'' such that cloud formation above the outflow leading edge was eliminated along with the associated storm induced subcloud convergence. The results from both of these simulations were qualitatively and quantitatively contrasted with the baseline simulation, hereafter referred to as ''BASE.''

3. Evolution of the NST family and associated deep convection

a. Misocyclone and initial tornado development

The simulated outflow originates from the collapse of the cold pool reservoir, yielding a thunderstorm outflowlike density current as in LW97. As the outflow propagates eastward and encounters the region of low-level southerlies, significant horizontal shear is realized across the current's leading edge, setting up a vertical vortex sheet (note that the winds within the outflow body are predominantly westerly). Regions of marked horizontal shear similar to that created in this simulation and aligned along boundary layer convergence lines are evident in observational NST studies (Wilson 1986; BS89; WW89; Wilczak et al. 1992; RW95). The captivating part of the initial NSTG process lies not with the development of this vortex sheet but with its breakdown into horizontal shearing instabilities that are the inaugural circulations of developing misocyclones along the outflow leading edge. This vortex sheet breakdown is illustrated in the plan view perspective of vertical vorticity provided in Fig. 3 for selected times in the BASE simulation. The vortex sheet, fully developed by 900 s, begins breaking down into individual instabilities of which nine are evident by 1020 s. These horizontal shearing instabilities are triggered by the subtle three-dimensionality provided by a weak lobe and cleft instability response at the outflow leading edge and any residual signal remaining from the small thermal perturbations initially present at the leading edge of the cold pool. Lobe and cleft instability develops in the gravitationally unstable region at a density current's leading edge where less dense ambient air is overrun by the current and attempts to rise up through the current's nose, creating a pattern of lobes and clefts (see Fig. 5 in LW97; Simpson 1972). The evolution of this vortex sheet into a line of misocyclones proceeds in the same manner documented in the dry simulations of LW97. From 900 to 1140 s, vortex sheet roll up is evident as the developing horizontal shearing instabilities of approximate 1.3-km wavelength create a clear pattern of vorticity rich and poor areas generated by preferential advection of cyclonic vertical vorticity along the sheet into the developing pools of vorticity. During this same period, selective amplification of the

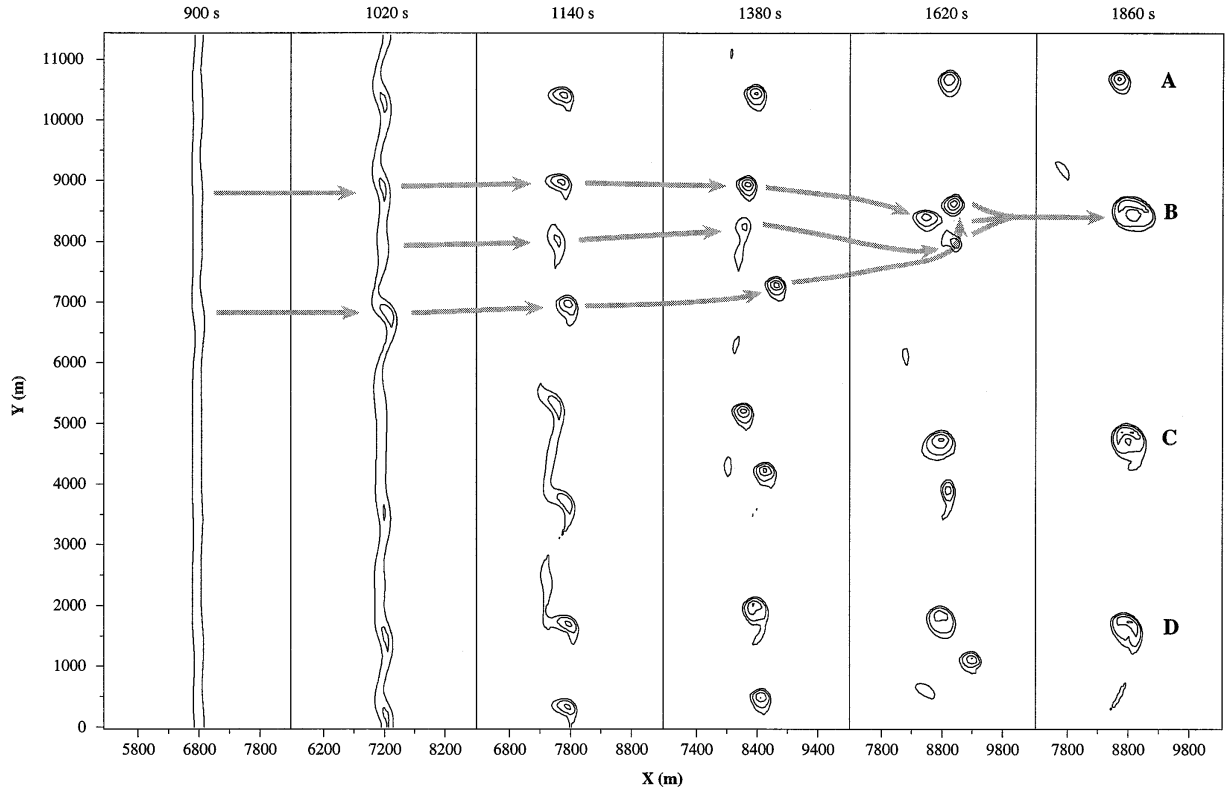

FIG. 3. Time sequence of the outflow leading edge surface vertical vorticity. Vertical vorticity contours plotted are 0.05, 0.1, 0.2, and 0.3 s^{-1}. The gray arrows represent misocyclone paths from one time sequence to another.

fastest growing available modes determine the resulting pattern of vorticity maxima (Batchelor 1967). A beautiful observational example of this leading edge roll up may be found in a study by Mueller and Carbone (1987) that looked at the dynamics of a thunderstorm outflow transiting the Denver area on 19 June 1984. Note that, since a box speed in the north–south direction has been tuned to the average northerly motion of the vortices ($\sim$7.5 m s^{-1}), the vortices appear to have no northward motion in Fig. 3. Subharmonic interactions ongoing along the leading edge between 1020 and 1860 s result in 1) vortex pairing events between vortices of similar strength that lead to vortex pair coalescence, and 2) extrusion events in which a stronger vortex extrudes the vorticity from its weaker neighbor(s). All of these processes ultimately result in the concentration of vertical vorticity and the increase in circulation at four discrete locations along the outflow leading edge by 1860 s. To visually trace the consolidation of vertical vorticity along one section of the vortex sheet into the longer wavelength pattern ($\lambda \sim 3$ km) seen at 1860 s, gray paths in Fig. 3 may be followed from the original incipient instabilities to the large consolidated vortex located at $y = 8500$ m. Note that the process of concentrating vorticity along the sheet into the four major misocyclones occurs over relatively short timescales ($\sim$15–20 min). The larger-scale entities at 1860 s, hereafter designated as vortex/NST A, B, C, or D, shown in Fig. 3, represent a concentration of eddy kinetic energy along the leading edge. The reader is referred to LW97 for a detailed look at the vortex dynamics of this misocyclone generation process. The merger of vortices seen here shares much in common with the two-dimensional simulations of perturbed vortex sheets by Riley and Metcalf (1980) and Corcos and Sherman (1984). Additionally, the coalescence processes involving these like-signed vortices are similar to those found by McWilliams (1984) for isolated coherent vortices in two-dimensional turbulent flow. Convergence line misocyclone circulations that have been suggested to arise from horizontal shearing instability similar to that modeled here have been reported in observational NST studies (and studies of other related vortices along convergence lines) by Carbone (1983), Wilson (1986), Mueller and Carbone (1987), BS89, WW89, and RW95. Note that since initial vortex sheet roll up and subsequent interactions take place on scales that are quite small ($\sim$1 km), many radar and numerical studies featuring boundaries possessing marked horizontal shear never resolve these phenomena.

To gain a three-dimensional perspective of the ensemble evolution of the developing line of deep convection, the outflow boundary, and the misocyclones and initial NSTs, Fig. 4 is provided. The perspective of the first three panels of Fig. 4 for times 1260, 1440, and

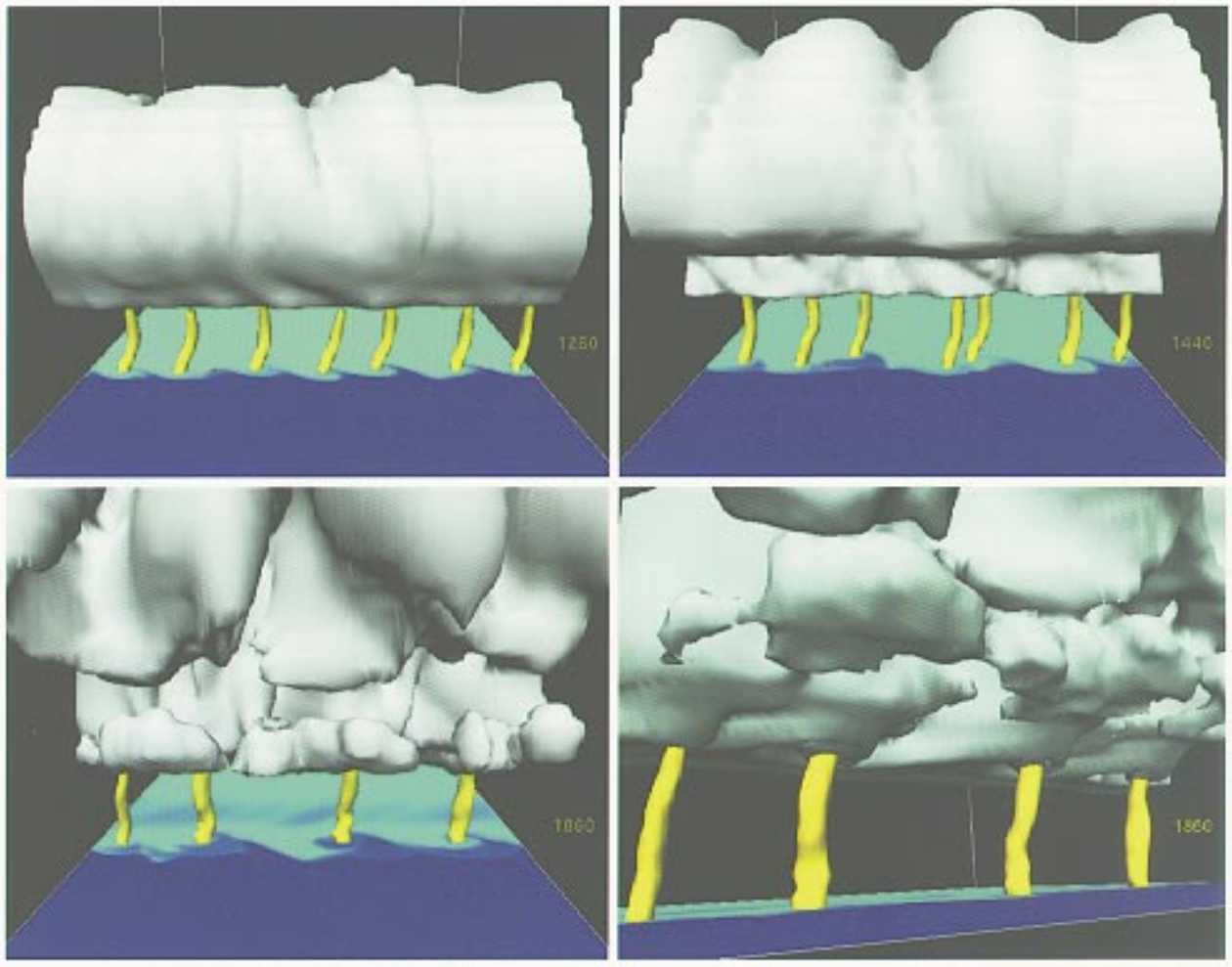

FIG. 4. Three-dimensional model renderings of the evolving ensemble of leading edge vortices, storm, and outflow boundary for 1260, 1440, and 1860 s. At the domain base the blue color spectrum delineates the outflow boundary (darker = colder). The yellow vertical vortex tubes are representative of vertical vorticity greater than 0.1 s^{-1}. The gray-scaled cloud isosurface represents cloud water greater than 0.2 g kg^{-1}. Viewing perspective in the first three panels is from an elevated position looking east, while the viewing position in the fourth panel is surface-based, looking southeast.

1860 s is from an elevated position looking east. At 1260 s, a gradually deepening line of moist convection (maximum cloud top of 6.5 km) has initiated over the outflow leading edge. Lying underneath this line of convection, misocyclone cores represented by the shallow (but rapidly deepening) vortex tubes are tied directly to the leading edge of the outflow boundary, delineated by the sharp coloration change from cyan to dark blue. At this time, there are seven prominent misocyclone circulations denoted by the vortex tubes and one weak circulation located between the second and third principal circulations from the left (the weak vortex patch at $y = 8000$ m seen at 1140 s in Fig. 3). The misocyclone circulations may additionally be inferred from the wave pattern in the outflow leading edge thermal structure created by the cyclonic advection of cool outflow air around the misocyclones. By 1440 s, the rightmost six principal misocyclones are observed to pair off, while, concurrently, the line of rapidly deepening convection takes on a much more three-dimensional character with towers reaching the 8.5-km level. Misocyclone merger events have been observed just prior to NST occurrences on at least three occasions (Wilson 1986; Wilczak et al. 1992; RW95). Animations of the model vorticity fields and massive particle trajectory releases indicate that this merger process between vortices first takes place in the convergent flow in the lowest few kilometers followed by a gradual consolidation at higher levels.[1] By 1860 s,

[1] *Visualization of a Numerically Simulated Family of "Landspout" Tornadoes Along a Weak Outflow Boundary* is a 7-min video produced at NCSA featuring the simulation analyzed in this article. Copies are available from the authors upon request.

FIG. 5. Photograph of three of six simultaneously occurring NSTs reported near Lazbuddie, Texas, on 4 June 1995. (Photograph copyright P. Blottman).

a family of young NSTs is apparent, with three of these circulations resulting from misocyclone coalescence events. Vortices B, C, and D now qualify as young NSTs, while the winds in vortex A fall just below NST threshold intensity (as defined in section 1) until they exceed it at 2280 s. The model-rendered tornado family is visually comparable to outbreaks of NSTs orientated in a vortex row configuration such as pictured in Fig. 5. The storms exhibit marked three-dimensional character at 1860 s, with three large convective towers that have reached an altitude of 10.5 km. The last panel in Fig. 4 provides a ground-based close-up perspective looking southeast at the young NST family and cloud base. Notable in this image is the major restructuring of the cloud base by the deepening misocyclone circulations. Encircling each vortex tube is a ''collarlike'' cloud with a slightly lowered cloud base that is further bounded by a dry slot created from the entrainment of nonsaturated air into the circulation at levels above cloud base. Animations of the simulation from this ground-based perspective distinctly show the upward progression of these originally shallow circulations (via the ascending vortex tubes) and clearly shows cloud-base motion reflecting these deepening circulations. The collarlike cloud-base structure and associated rotating ''swirl'' appearance in the cloud base may be comparable to similar cloud-base appearance reported in observational NST studies (BS89; WW89) and in some waterspout observations (Golden 1971). In section 4, a detailed analysis of the development and demise of the NST B member of this tornado family is provided.

At low levels, a very coherent signal of the young NSTs at 1860 s may be seen in the model wind, vorticity, and pressure fields in Fig. 6. Much similarity exists between the southernmost vortices (B, C, D), which are all products of misocyclone mergers, in stark contrast to the small northern vortex at $y = 10\,600$ m. As seen in the surface misocyclone-relative horizontal wind field, the vortex diameters, designated as the across-circulation diameter of the annulus of peak wind speed, ranged from 300 m for the small northern vortex to an average of 550 m for the southern three circulations. To put these dimensions in perspective, WW89 and Wakimoto and Martner (1992) have reported photogrammetrically retrieved NST widths ranging from 25 to 600 m. At this initial NST stage, peak vertical vorticity was approximately 0.3 s^{-1} for all four vortices; however, the distribution of vorticity differed markedly from the vortex ring pattern seen for the young NSTs B and C to a more centralized vorticity maximum for vortex A and NST D. The surface pressure field in Fig. 6 has approximately cyclostrophically adjusted to the NST low-level rotations, as may be seen using Eq. (1) below:

$$\Delta p \sim \rho V_t^2. \tag{1}$$

Assuming an average tangential velocity (V_t) for NSTs B, C, and D of 21 m s^{-1} and a density (ρ) of 1.03 kg m^{-3} for the near-surface environment, the expected perturbation pressure deficit is 4.5 mb, a value close to the average pressure deficit observed of 4.6 mb (calculated with respect to the pressure field just outside the circulation proper). The vertical velocity field at the 250-m level shown in Fig. 6 features updraft regions encircling the vortices with peak updraft of approximately 7 m s^{-1}

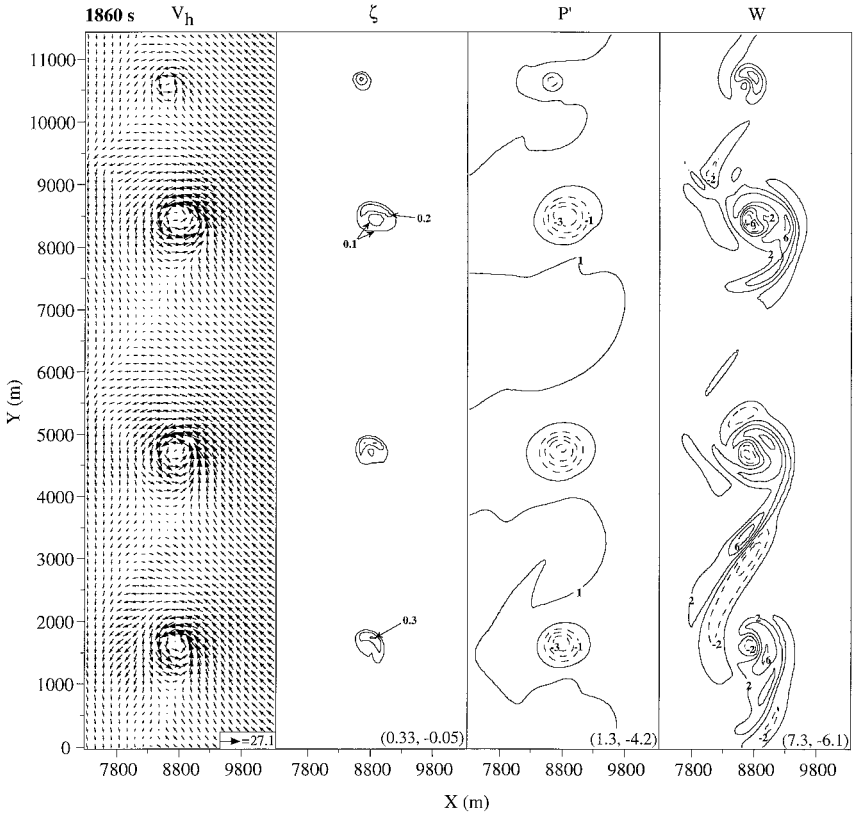

FIG. 6. Horizontal cross sections at 1860 s of the misocyclone-relative horizontal surface wind (V_h), positive surface vertical vorticity (ζ), surface perturbation pressure (P'), and 250-m vertical velocity (W). Contour intervals are 0.1 s^{-1}, 1 mb, and 2 m s^{-1} for the vertical vorticity, perturbation pressure, and vertical velocity plots, respectively. Maximum velocity vector (m s^{-1}) and field maxima and minima are shown in the lower right corner.

located along the eastern periphery of each young NST. Most interesting perhaps is the presence of an axial downdraft at this level in each of the vortices except vortex A. The largest axial downdrafts exist in NSTs B (-6.1 m s^{-1}) and C (-4.5 m s^{-1}) and their existence may explain the ringlike vorticity distribution seen for these NSTs. As the downward axial flow nears the surface, a local divergence region results (and a region of negative vortex stretching), creating the vortex ring and generally wider circulation. These axial downdrafts will be examined in greater detail in section 3c.

b. Development of moist convective asymmetry

Previous dry and moist simulations of misocyclone evolution along outflow boundaries have indicated that these circulations have a marked influence on the updraft distribution along the outflow leading edge and should correspondingly affect the spatial distribution of deep convection developing there (Lee 1994; LW97). Kingsmill (1995) suggested the possibility that misocyclones along an outflow boundary could initiate deep convection but was unable to verify this hypothesis in an observational study using a 1991 Convection and Precipitation/Electrification Project dataset from Florida. In light of these previous modeling results, Kingsmill's hypothesis appears to be justified. Model evidence indicates that the misocyclones do strongly influence storm structure. Figure 7a shows the cloud-base updraft at the 2-km level at 1860 s. The major misocyclones have strikingly altered the updraft distribution with ''hook''-shaped updraft appendages wrapping well around the misocyclone circulations at this level. This pattern is consistent with the slotted moist convective collar seen in the ground-based perspective of the fourth panel of Fig. 4 and is the cloud-base reflection of a moist convective plume that nearly encircles the misocyclone circulation up to the midlevels of this storm complex. A very narrow and weak axial downdraft may be seen for NST B even at cloud-base level. Beginning around 1860 s, rain wrapping around the deepening major misocyclone circulations is also being configured in hook patterns (corresponding to the slot of updraft minima to the inside of the updraft hooks) that notably resemble in size and shape the radar reflectivity hooks documented by RW95 for one of the NSTs which occurred in the 15 June 1988 Denver NST outbreak (see their Fig. 8). Radar hook echoes, normally associated

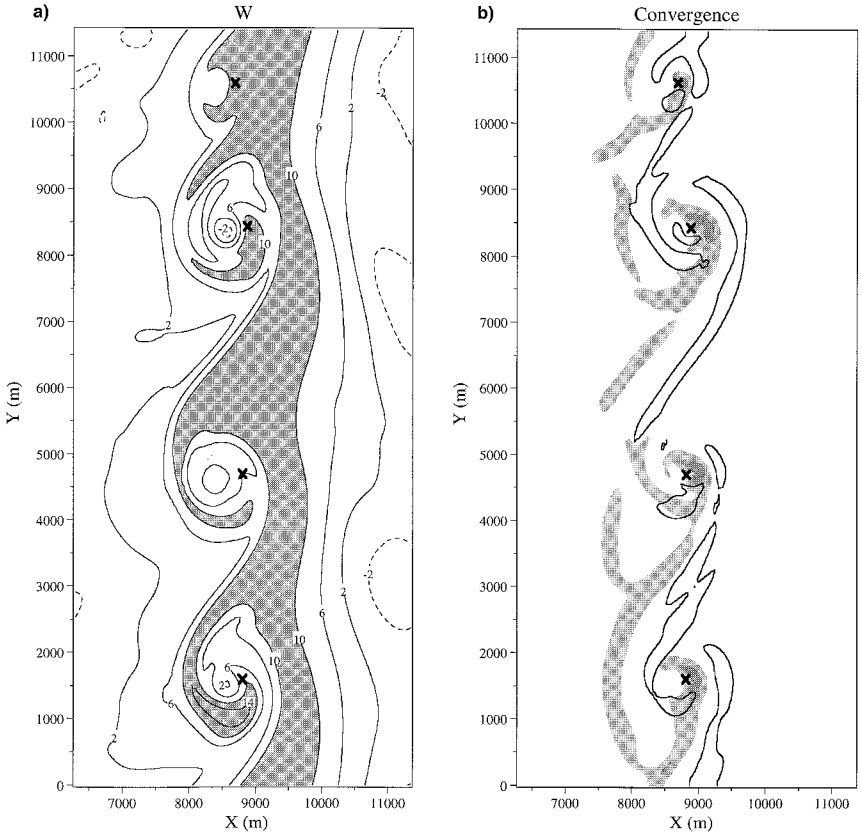

FIG. 7. Horizontal cross sections at 1860 s of (a) vertical velocity at 2000 m (cloud base) and (b) convergence at both the surface and at 500 m. (a) The dark shading denotes areas of updraft greater than 10 m s^{-1} and the **x**'s show the positions of the circulation centers at the surface. The vertical velocity contour interval is 4 m s^{-1}. (b) The light gray shading denotes surface convergence greater than 0.01 s^{-1} and the dark shading represents surface convergence greater than 0.05 s^{-1}. The heavy solid line in (b) represents convergence greater than 0.01 s^{-1} at the 500-m level.

with supercellular convection, have also been reported with other NST events (Wilson 1986; WW89; Wakimoto and Martner 1992) and additionally in waterspout cases (Golden 1974b; Golden and Sabones 1991).

To understand the boundary layer forcing driving, in part, the pattern of updrafts seen in Fig. 7a, plots of convergence at the surface and at the 500-m level are provided in Fig. 7b. Surface convergence of greater than 0.01 s^{-1} nearly encircle the vortices, with values larger than 0.05 s^{-1} found along the eastern side of the circulations. This low-level convergence pattern is principally produced by surface friction-induced radial inflow. This convergent forcing around the low-level misocyclone directly sustains the columnar updraft at low levels, which ultimately supports the moist convection above the boundary layer NST circulations. Concurrently, the moist convection is providing a positive feedback by inducing local convergence into the subcloud layer above the misocyclones; thus, both mechanisms work cooperatively in supporting a deep misocyclone updraft column. The deep convective updrafts between and to the east of the misocyclones at cloud base appear better associated with the convergence pattern at 500 m, seen in Fig. 7b. This convergence pattern is positioned along the vertical thermal wall of the outflow boundary.

To shed further light on the convective forcing along the line, time-dependent misocyclone-relative trajectory studies for the period between 1500 and 1900 s (i.e., the period of final merger for the vortex pairs and marked reconfiguration of the deepening convection) were run to identify the source regions supporting the storm and updraft profiles seen in Figs. 4 and 7a. The trajectory analysis uses stored three-dimensional model datasets at 20 s intervals and employs a fourth-order Runge–Kutta method for the time integration of the trajectories. Forty-six trajectories (every fourth grid point) were laid out in a north–south line approximately 400 m east of the row of misocyclones along a path from $y = 200$ to 11 200 m and at an elevation of 200 m, as shown in Fig. 8. Most of the trajectories become entrained in the low-level convergent flow field surrounding the misocyclones and then rise rapidly in the strong boundary layer updrafts that the misocyclones and over-

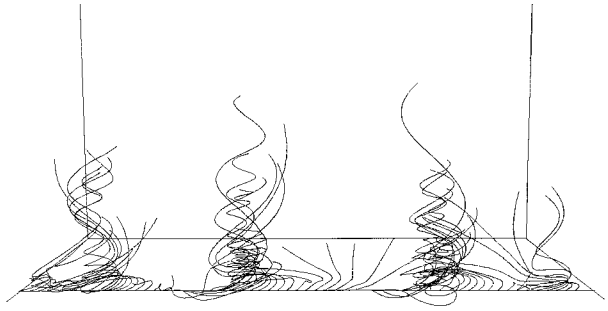

FIG. 8. Time-dependent trajectories released at $z = 200$ m and at a position 400 m to the east of the row of vortices. Forty-six trajectories were tracked from 1500 to 1900 s. The perspective is from an elevated position looking west. The tallest trajectory at 1900 s has reached the 4200-m level.

head moist convection are driving. Clearly, the moist convection just above the misocyclones is being supported by air at low levels in the boundary layer that is drawn into the misocyclone circulations and lifted. Slightly lowered cloud bases directly above the organizing misocyclone circulations would further suggest that this moist convection is tapping into air originating just above the surface, which is slightly more moist. Note that, in this simulation, rotationally induced pressure deficit is not accounted for in the model saturation vapor pressure calculation; thus, no pressure-induced cloud lowerings are possible in the model as configured. To put the trajectory endpoint heights in Fig. 8 in proper perspective, the highest trajectory has ascended to 4200 m between 1500 and 1900 s. Trajectories that do not become entrained in the misocyclone flow fields such as those between the middle two misocyclones rise comparatively very little during this time. To further investigate the source regions for air supporting the moist convection, a backward time-dependent trajectory analysis was conducted at 1900 s with a line of trajectories released along a line parallel to cloud base at cloud-base level (2000 m). During a 400-s time integration, this analysis demonstrated that the air feeding the moist convection between the misocyclones largely originated at elevations higher in the boundary layer and much farther upstream than the air supporting the moist convection atop the misocyclones. Parcels associated with these trajectory paths between the misocyclones rose slowly in the boundary layer until encountering the outflow wall between the misocyclones, at which point the parcels ascended rapidly to cloud base. This pattern of deep convective forcing near the misocyclone proper and along the outflow boundary thermal wall just north of the misocyclones is consistent with the dry simulation results of LW97. An in-depth numerical study of deep moist convective forcing by misocyclone circulations is currently under way.

c. Tornado maturity and dissipation

The NSTs display generally steady character between 1860 and 2000 s, after which marked changes in appearance and intensity take place as new outflow from the line of storms begins to influence the circulations. Figure 9 is provided for a three-dimensional perspective of key stages in the maturation and dissipation of the NSTs. This visualization employs both the three-dimensional isosurface renderings used in Fig. 4 and a colored massive particle trajectory release to yield qualitative information on the vortex structure and vertical velocity character. At 1980 s, the line of vortices is very similar to that seen in Fig. 4 for 1860 s (using the same viewing perspective). The NST family members are vertically erect and situated along distinct open waves apparent in the surface temperature field, which result from misocyclones aligned along the original outflow leading edge. The NSTs also have very similar dimensions and intensity as seen at 1860 s in Fig. 6. The first region of new outflow reaching the surface is indicated by the dark blue area just to the east of the NST family at 1980 s. New outflow, originating principally from the cooling created from evaporating precipitation, continues to descend and spread out along the surface both to the east and west of the vortex row. Concurrent with this introduction of new cold pools bounding the NSTs, the vortices narrow and intensify markedly. The second panel of Fig. 9 for 2160 s displays a snapshot visualization from a massive particle release, whereby 6500 particles were introduced at locations along the outflow leading edge where the vertical vorticity exceeded 0.04 s^{-1}, starting at 1200 s. The perspective here (and in the fourth panel) is looking southwest from an elevated position. The green coloration is used for particles in updraft and the red coloration for particles in downdraft. For a proper height perspective, particles at the very top of this picture are at the approximate 6500-m level. This visualization reveals very coherent vortex structure with most particles in updraft at this time; however, note the stream of red particles in the center of NSTs B, C, and D. This stream of particles is aligned along an intensifying axial downdraft developing in these three strong vortices. In contrast, the more narrow and sinuous vortex A displays only updraft character through most of its existence. By 2200 s (panel 3), the new cold pools are indicated by the expanding dark blue regions wrapping around the periphery of the NST circulations. Note that, in this visualization, a temperature-relative coloration technique is employed at the domain surface such that the coldest temperatures at any particular time are colored with the darkest blue shading. By 2200 s, some of the new cold pools have maximum perturbation potential temperature deficits at their center of -8 K. At this stage, the vortex intensity is nearing its peak. As this storm–NST system becomes more outflow dominated, especially after 2360 s, three of the vortices become highly tilted, as shown in the massive particle visualization for 2504 s. Their low-level portions get undercut and advected by the strongest nearby cold pool in a similar fashion to that documented for a Colorado NST occurring on 2 June 1987 (Wakimoto and Martner

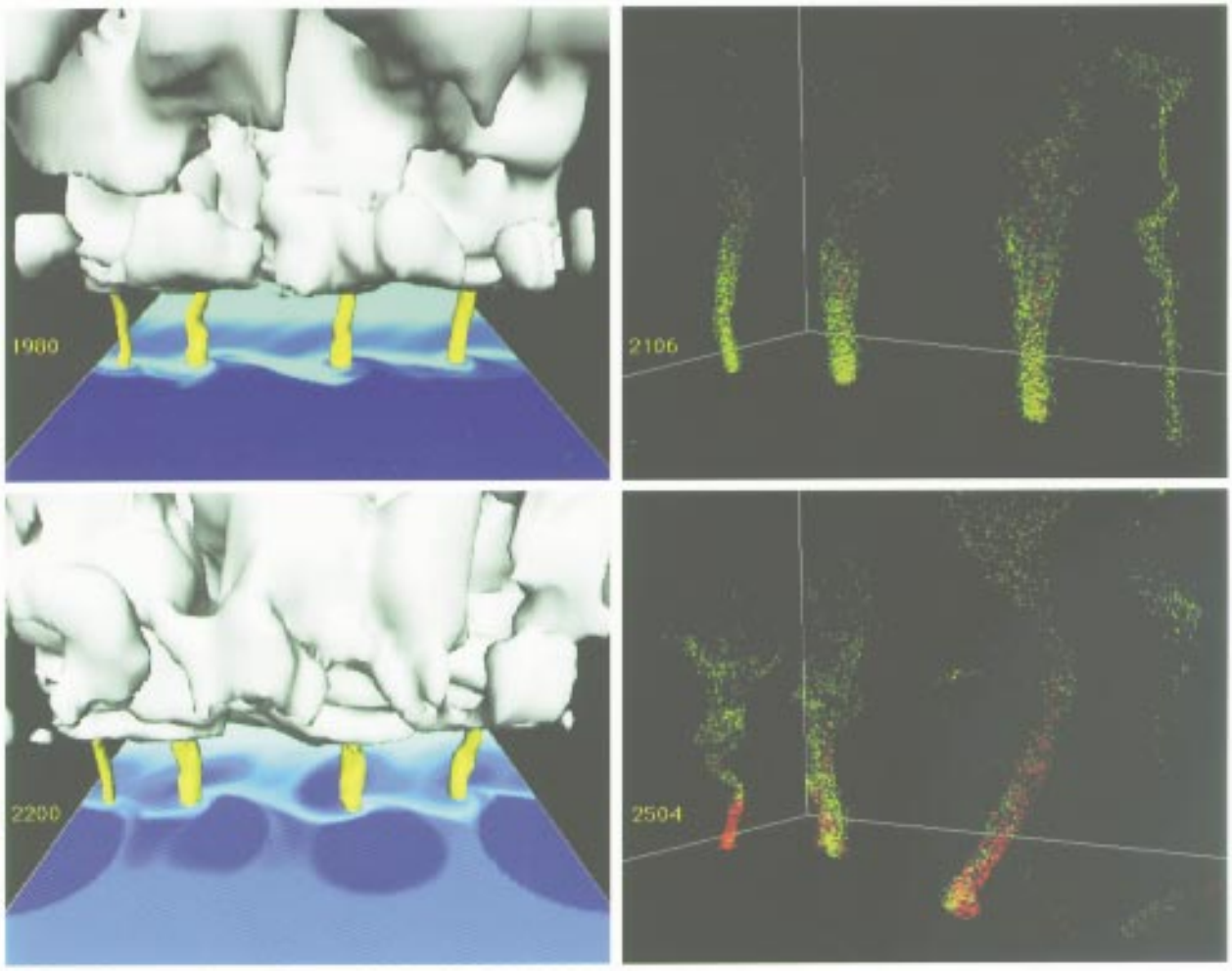

FIG. 9. Three-dimensional model renderings for times 1980 and 2200 s using the same criteria as in Fig. 4. Massive particle trajectory visualization is shown for times 2106 and 2504 s with a perspective looking southwest from an elevated position. The green and red color coding for the 6500 particles represents updraft and downdraft, respectively (see text for further details).

1992). These highly tilted vortices create a ''roping out'' appearance quite common in the dissipation stages of both nonsupercell and supercell tornadoes. Note that, by 2504 s, red particles denoting downdraft make up a large percentage of the total particles displayed, indicating that the cold negatively buoyant flow of the new cold pools has wrapped around the tornadic circulations, dissipating the low-level updrafts almost completely. The NST intensities continue to decline until the simulation's end at 2640 s.

A comparative examination of the NST family's low-level features between 1860 s, shown in Fig. 6, and at 2200 s, a time near maximum intensity shown in Fig. 10, reveals major changes in the local flow regime in which the vortices reside, along with a marked change in vortex size and intensity. The average diameter by 2200 s of the major NSTs (B, C, D) is approximately 400 m with the diameter of vortices B and D contracting about 30% since 1860 s. The principal flow regime change occurring after 2000 s involved the introduction of new storm outflow regions into the low-level environment, seen as distinct divergence areas in the surface horizontal wind field. The configuration of the primary outflow divergence areas relative to the tornadic circulations for vortices B and C resembles the wrapping rear-flank downdraft portion of the classic Lemon and Doswell (1979) schematic of the low-level flow structure of supercell thunderstorms, albeit on a smaller scale (see their Fig. 7). RW95 suggested that the interaction of new outflow with a misocyclone circulation similar to that modeled here was instrumental in vortex intensification for one of the 15 June 1988 Denver, Colorado, NSTs. Carbone (1983) reported on a case of NSTG along a severe cold frontal rainband where the observed tornado occurred at a time coincident with the appearance of nearby spreading downdraft close to the surface. In this simulation, the three major NSTs were already under way for 3–4 min before new outflow pools in-

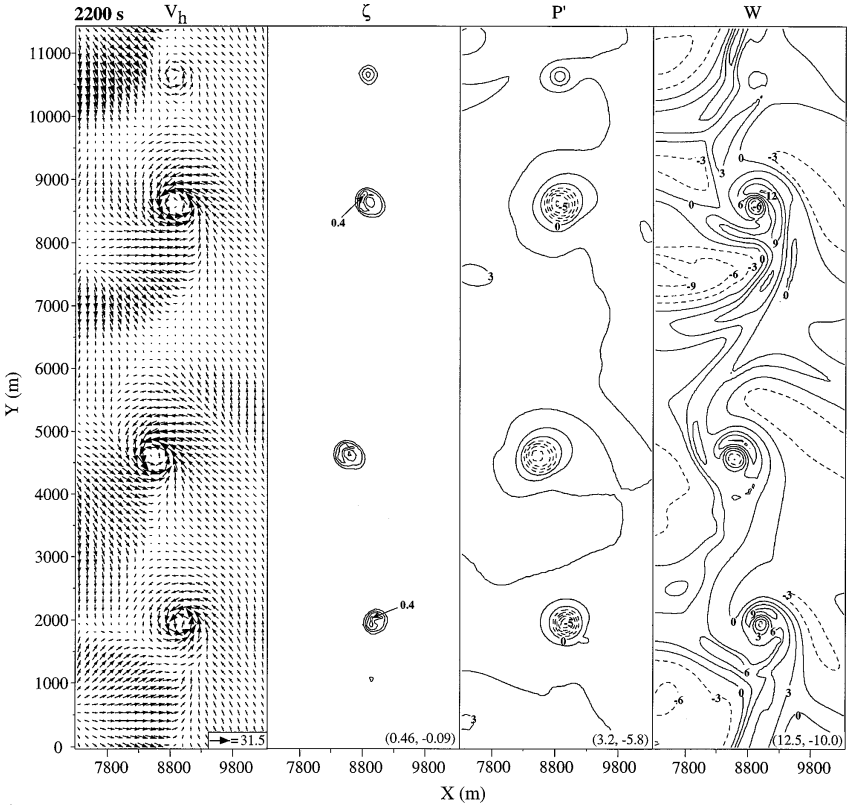

FIG. 10. Horizontal cross sections at 2200 s of the NST-relative horizontal surface wind (V_h), positive surface vertical vorticity (ζ), surface perturbation pressure (P'), and 250-m vertical velocity (W). Contour intervals are 0.1 s^{-1}, 1 mb, and 3 m s^{-1} for the vertical vorticity, perturbation pressure, and vertical velocity plots, respectively. Maximum velocity vector (m s^{-1}) and field maxima and minima are shown in the lower right corner.

teracted with these vortices, so that the primary role of the outflow here is in the intensification of the NSTs. The major vortices reach F1 intensity soon after these outflows begin to encounter the surface circulations with peak ground relative surface wind speed of 39 m s^{-1} realized for NST B at 2280 s. Concurrent with the outflow–vortex interactions, surface vertical vorticity at 2200 s jumps to near 0.4 s^{-1} in NST C and over 0.4 s^{-1} for NSTs B and D, while the surface pressure drops accordingly within these vortices to a maximum pressure deficit of approximately 7 mb (with respect to the pressure field just outside the circulation proper). The vertical velocity patterns associated with the major NSTs at 250 m have contracted in size and nearly doubled in intensity, while the axial downdrafts have strengthened slightly while narrowing significantly. In contrast, the updraft region for NST A has nearly disappeared, signaling the end of its intensification. Peak 250-m updraft and axial downdraft at this time are associated with NST B and are 12.5 and −6.5 m s^{-1}, respectively. As seen in Fig. 6, the surface vortex ring pattern displayed by NSTs B and C at 1860 s also exists at 2200 s and is the result of the axial downdrafts penetrating to near the surface. Note the presence of wrapping, precipitation-driven downdrafts both west and east of the major NSTs that are driving the new cold pools at the surface.

The X–Z vertical plane through NST B shown in Fig. 11 at 2200 s reveals a 5000-m-deep axial downdraft with a surrounding updraft annulus reaching the storm midlevels. The vortex column is of similar depth, as revealed by the shaded region in Fig. 11. The vertical velocity structure at low levels resembles the high swirl ratio two-cell vortex model schematic of Davies-Jones (1986) with a penetrating downdraft to the surface. To examine the forcing mechanisms driving the low-level portion of this axial downdraft, the inviscid Boussinesq approximation of the vertical momentum equation [Eq. (2)] is examined for a section of the NST B axial downdraft,

$$\frac{\partial w}{\partial t} = -\mathbf{V}\cdot\nabla w - \frac{1}{\overline{\rho}}\frac{\partial p'}{\partial z} + g\left(\frac{\theta'}{\overline{\theta}} + 0.61q_v' - q_c - q_r\right) \quad (2)$$

between 500 and 1000 m at 2200 s. The first two right-hand side terms of Eq. (2) represent the change in vertical velocity at a given point due to advection and the perturbation pressure gradient force. The third term rep-

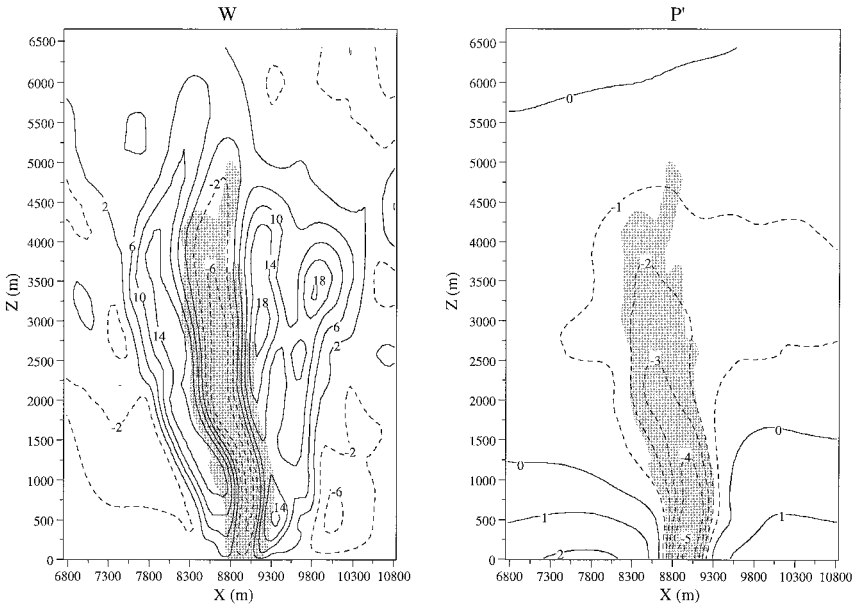

FIG. 11. Vertical *X–Z* slice of vertical velocity (*W*), perturbation pressure (*P′*) and vertical vorticity (ζ) through the center of NST B at 2200 s. The gray background profiles represent areas where the vertical vorticity is greater than 0.04 s^{-1}. Contour intervals are 4 m s^{-1} and 1 mb for the vertical velocity and pressure fields, respectively.

resents the virtual buoyancy and water loading. For this analysis, the first term can be further simplified by considering only the vertical advection of *w* since the vortex-relative radial flow vanishes near the vortex axis. The third term can also be simplified given that no cloud water exists in this layer and negligible rainwater had yet been entrained into the low-level vortex. The results of this analysis revealed that the layer average perturbation pressure gradient term (-0.150 m s^{-2}) was an order of magnitude larger than the layer average buoyancy term (-0.015 m s^{-2}) and two orders of magnitude larger than the layer average advection term ($-$ 0.003 m s^{-2}). Thus, the downward-directed perturbation pressure gradient force induced by strong low-level rotation [Eq. (1)] is primarily responsible for the low-level axial downdraft. A comparison of the vertical acceleration forcing term magnitudes higher in the vortex column similarly reveals that the perturbation pressure gradient term remains dominant. The plot of perturbation pressure (referenced from the base state) in Fig. 11 demonstrates that a local reversal in the vertical perturbation pressure gradient along the axis of the NST extends from the surface to above the 4000-m level. Axial downdrafts in tornadoes have been observationally documented using Doppler radar (Wakimoto and Martner 1992; Wurman et al. 1996) and have been indicated in two- and three-dimensional numerical models of tornado-like vortices such as in Walko (1988) and Lewellen et al. (1997), respectively.

The minimum contracted vortex diameters at the surface for the major NSTs after 2200 s are constrained by the balance between surface inflow convergence and core divergence provided by the penetrating axial downdrafts that reach nearly to the surface. Additionally, the diameter and character of the NSTs as the vortices approach and, in some cases, fall below 360 m in diameter (NSTs A and D) are highly limited by the model horizontal resolution with the 60-m grid. At these narrow diameters, the tight model field gradients induce high values of model mixing that acts to relax the gradients and consequently constrain the real minimum diameter and model field variable maxima and minima of these NSTs. Additionally, to approach a low-level vortex solution with fidelity, much finer grid spacing ($\sim$10 m) may be required, as suggested by Lewellen (1993).

Despite the resolution limitations noted above, the dissipation of the NST family can still be qualitatively represented. The decay of the simulated NSTs, well under way for all member vortices by 2460 s, occurs as the low-level flow field becomes increasingly dominated by outflow from the storm complex. The surface vortex-relative wind field at this time, shown in Fig. 12, is characterized by numerous divergence regions associated with the descending storm outflow. Regions of strong outflow have moved the low-level NST circulations well off the family's north–south axis seen in Fig. 10, resulting in highly tilted vortex tubes similar to that photogrammetrically documented for a Colorado NST by Wakimoto and Martner (1992). Concurrently, substantial reductions since 2200 s in average surface peak vertical vorticity (36%) and average peak pressure deficit (47%) have occurred as the rotation weakens in the dying family of NSTs. In stark contrast to the well-organized vertical velocity structure seen at 2200 s, the

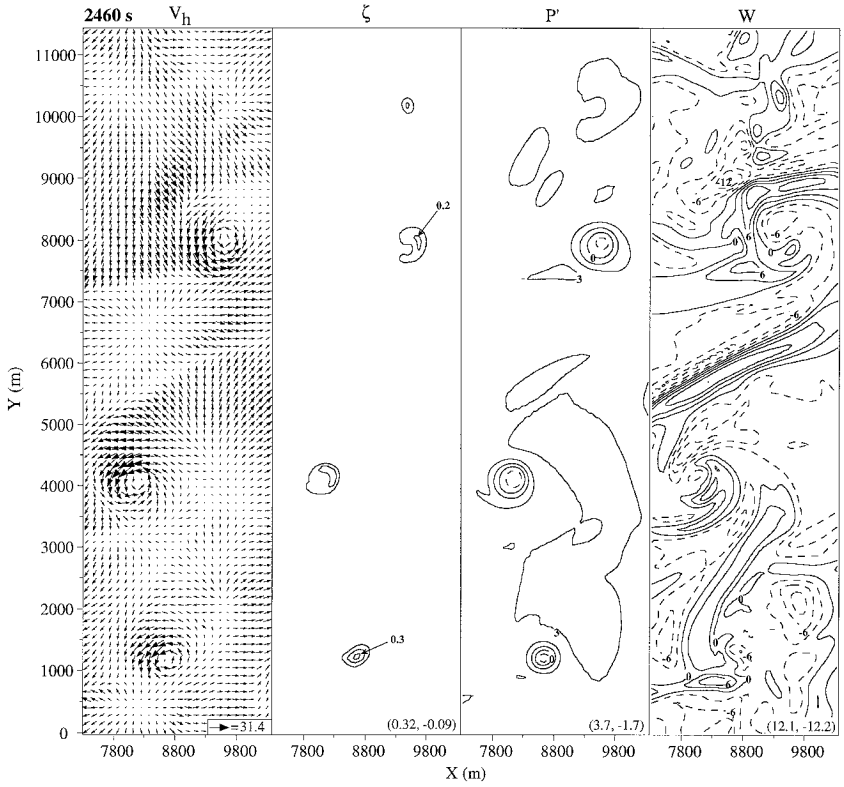

FIG. 12. As in Fig. 10 except at 2460 s.

pattern of vertical velocity at 2460 s is complex, with downdrafts predominating. Cold and negatively buoyant downdraft air is quickly surrounding and becoming entrained into the major low-level circulations, leaving a good portion of the vortex in descending and divergent motion. This dissipation process, brought about by the introduction of stable air, is much like that described in the demise of waterspouts (Golden 1974a; Wakimoto and Lew 1993) and of observed low-level mesocyclones in tornadic supercell thunderstorms by Brandes (1984). Further, this process appears qualitatively similar to the dissipation of the Dimmit, Texas, tornado of 2 June 1995 reported by Rasmussen and Straka (1996).

4. Analysis of the life cycle of NST B

a. Time series analysis

To elucidate the developmental stages of a typical NST as simulated here, various time-series analyses have been completed using representative vortex B. Time–height cross sections for maximum vertical vorticity and vertical velocity shown in Fig. 13 have been created by extracting maximum values of these quantities throughout the model integration for each horizontal level in or very near the parent misocyclone circulation (or its predecessors) for NST B. A single-pass filter that averages each data point with its nearest neighbors (on all sides) has been applied to smooth out noise from this data. The most prominent gross feature seen in Fig. 13a for the vertical vorticity time series is its upward-sloping character out to approximately 1680 s, indicating the upward progression of vertical vorticity originating from the lower half of the boundary layer. This ascent of vertical vorticity is associated with a strong updraft pulse seen in Fig. 13b that is occurring nearly simultaneously within the juxtaposed developing deep moist convection. This upward vertical vorticity progression is consistent with the observations of WW89 and BS89. The prominent low- and midlevel cloud rotation observed in this simulation is a consequence of this upward transport of vertical vorticity from the boundary layer. During this period of vertical vorticity column deepening, low-level vorticity magnitudes are increasing markedly in the misocyclones. The vorticity time-height series in Fig. 13a is very similar in character to vorticity time–height cross sections compiled by RW95 for three of the NSTs occurring on 15 June 1988 near Denver, Colorado. In the case analyzed here, NST B was a product of misocyclone mergers around 1620 s into the simulation. This event shows up as a temporary drop in subcloud layer vertical vorticity magnitude in Fig. 13a at 1620 s. At this time of consolidation, vertical vorticity from the former individual misocyclones is redistributed to a larger diameter circulation, resulting in a drop in area average vorticity. A decline in peak vertical vorticity accompanies this

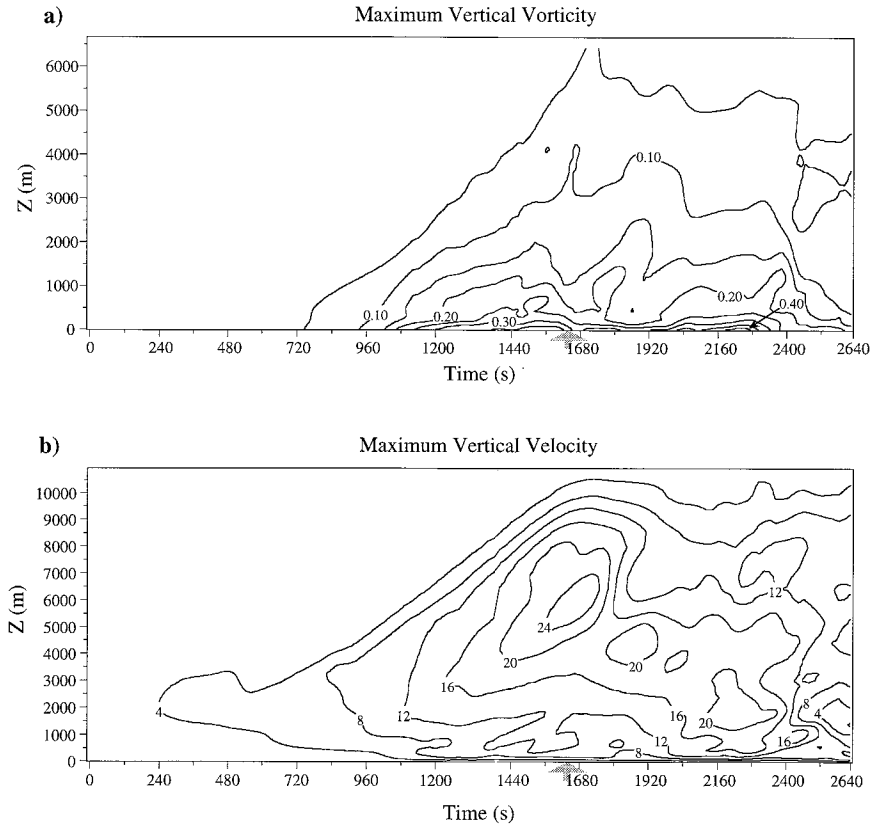

FIG. 13. Time–height cross sections of (a) maximum vertical vorticity and (b) maximum vertical velocity for regions in or near NST B and its predecessor misocyclones. Contour intervals are 0.05 s^{-1} and 4 m s^{-1} for the maximum vertical vorticity and maximum vertical velocity, respectively. The gray arrow marks the time of misocyclone coalescence.

drop in area-average vertical vorticity. An observational counterpart to the modeled NST B evolution is that documented by RW95 for their NST-designated T2. The parent misocyclone for T2 was the product of a misocyclone merger event not unlike that simulated here. During the merger process, Roberts and Wilson report an initial increase in diameter of the resultant vortex and a drop in vertical vorticity. A dual-Doppler-derived vertical vorticity time-height series reflects this temporary drop in vorticity during consolidation (see RW95's Fig. 13), much like the consolidation signal present in Fig. 13a at 1620 s, with both observational and modeled combined vortices showing strong subsequent intensification. The phase of strongest intensity for NST B spans the interval from 2000 to 2360 s, a period corresponding to the enhanced low-level vorticity seen in Fig. 13a. Not coincidentally, this period also includes the emergence of new low-level cold pools adjacent to the NST circulations that enhance the low-level convergence around the tornadic vortices. The signal of this period of maximum NST intensity is distinct in Fig. 13b as the 12 m s^{-1} updraft contour drops in altitude to near 200 m. A maximum low-level updraft of nearly 20 m s^{-1} is realized at the 500-m level at 2300 s. The period of marked NST dissipation is clearly delineated on both vertical vorticity and updraft series, beginning at approximately 2400 s. At this time, the depth of the intense vertical vorticity column drops substantially and the storm updraft decreases markedly. The time–height vorticity time series of RW95 also reflects this rapid decrease in depth and strength at NST dissipation. The demise of the modeled NSTs is due to the weakening storm in which updraft predominance has been replaced by downdraft predominance, while at the surface negatively buoyant and divergent outflow has inundated the environment in and around the dying NST circulations. This dissipation stage scenario is likely common for NSTs.

The life cycle stages of the NSTs in this simulation are well represented in time-series data of maximum surface vertical vorticity and circulation shown in Fig. 14 and in time series of maximum surface wind speed and pressure deficit shown in Fig. 15. This time series analysis focuses on the development of NST B. To construct Fig. 14, the maximum vertical vorticity was tracked initially for a section of the developing vortex sheet between $y = 6900$ and 10 200 m starting at 600 s, then subsequently for the misocyclones that devel-

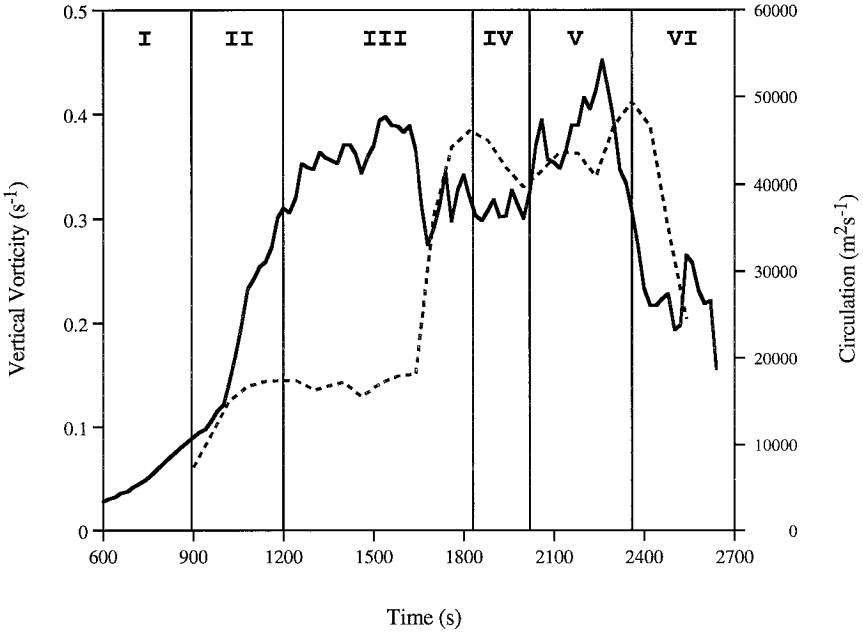

FIG. 14. Time series of maximum surface vertical vorticity (solid) and circulation (dashed) for the evolution of NST B. Life cycle stages overlaid on these time series are explained in the text.

oped from this section, and finally for the consolidated misocyclone that would produce NST B (see Fig. 3). The circulation time series was constructed starting at a time (900 s) corresponding to the appearance of a wave along the vortex sheet seen in Fig. 3 at $y = 7000$ m that would subsequently become one of the two primary misocyclones that later would merge to produce the parent misocyclone of NST B. The circulation was tracked through misocyclone merger and through the tornado life span. The circulation in the horizontal plane may be calculated using Eq. (3),

$$\Gamma = \overline{\zeta} A, \tag{3}$$

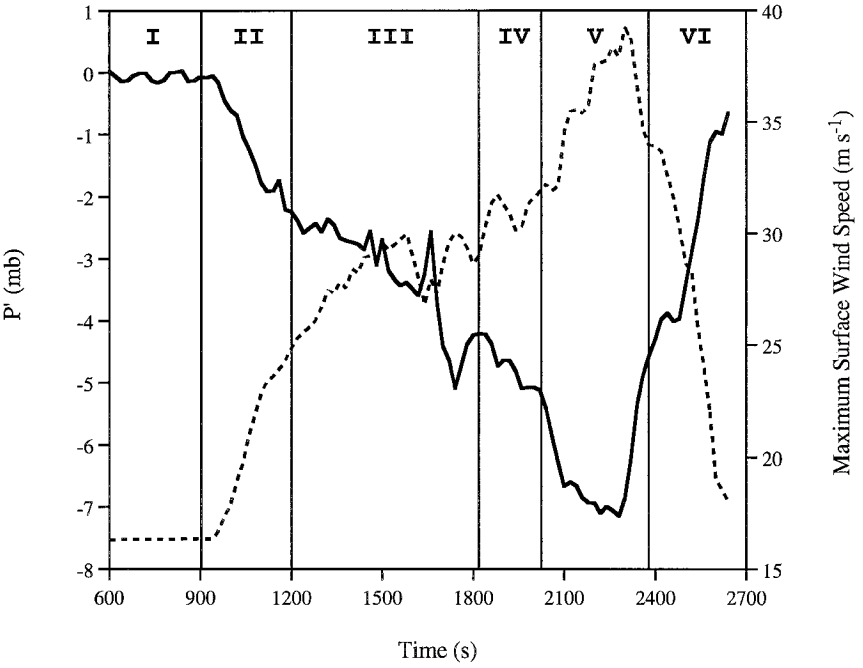

FIG. 15. Time series of maximum surface pressure deficit (with respect to the local surrounding environment, solid) and maximum ground-relative surface wind speed (dashed) for the evolution of NST B. Life cycle stages overlaid on these time series are explained in the text.

where $\overline{\zeta}$ is the average vorticity within some stated region *A.* For this calculation, the 0.01 s^{-1} vorticity contour for the chosen misocyclone is approximately encompassed by a box around which the circulation is computed. Based on the first part of this numerical study reported in LW97 and the results presented in section 3, six stages for the genesis, maturation, and dissipation of NSTs have been designated and are overlaid on the time series in Fig. 14. During the *vortex sheet development stage* (I) the gradual increase in vertical vorticity between 600 and 900 s is a consequence of the developing outflow boundary encountering the southerly wind regime. The *vortex sheet roll-up stage* (II) occurs between 900 and 1200 s (see Fig. 3). During this period, the peak misocyclone vertical vorticity has increased rapidly, while, correspondingly, the circulation has increased as vertical vorticity, originally nearly evenly distributed along the sheet, is concentrated in misocyclone centers. The *misocyclone interaction and merger stage* (III) spans the period from 1200 to 1820 s with circulation values that are nearly steady until approximately 1620 s when the circulation increases nearly threefold as the three vorticity concentrations seen at 1620 s in Fig. 3 merge by 1800 s. During this stage, the misocyclone peak vorticity continues to grow, although less rapidly than seen for stage II, reaching a maximum between 1540 and 1620 s, after which a sharp but short-term drop in vertical vorticity is observed, corresponding to the consolidation of the three vorticity concentrations. Vorticity values increase once again and then plateau out in the *NST early mature stage* (IV) that somewhat arbitrarily begins at 1820 s when NST B's maximum wind speed exceeds 30 m s^{-1} (see Fig. 15) and lasts until approximately 2000 s, at which time new outflow pools have emerged at low levels, creating additional convergence near NST B. In the *NST late mature stage* (V) beginning at 2000 s, NST B intensifies markedly in response to this outflow interaction with vertical vorticity values peaking at 0.45 s^{-1} at 2260 s. During both stages IV and V, the circulation for NST B fluctuates only slightly; however, similar to that observed in Fig. 13, the demise of NST B arises abruptly, as seen in the steep decline in both the circulation and vorticity curves during the *NST dissipation stage* (VI), which begins at approximately 2360 s.

Time series of peak pressure deficit and maximum ground-relative wind speed shown in Fig. 15 were created in a similar manner to the vertical vorticity time series of Fig. 14. Once again, the time series are overlaid with designated life cycle stages that reflect the tendency and magnitude of the time-series variables. The time-series plots for pressure and wind speed are near mirror reflections of each other (even in some of the minor details) and are clearly inversely correlated as anticipated for vortical flows via Eq. (1). Maximum winds and pressure deficits rapidly increase in stage II as small-scale misocyclones emerge along the outflow leading edge as the vortex sheet rolls up and closed circulations develop. In stage III, wind speeds and pressure deficits continue gradually increasing until the local flow fields are temporarily disrupted by the misocyclone mergers beginning at 1620 s. Once unification takes place, the pressure and wind fields quickly rebound with an immediate 2.5-mb drop in pressure and an increase in surface wind speed to 30 m s^{-1}. Stage IV is typified by slow intensification of NST B up to 2000 s, a time when the pressure deficit has reached 5.1 mb and the wind speed has reached 32 m s^{-1}. Consistent with the dramatic intensification indicated for vertical vorticity in Fig. 14 for stage V, the time series for wind speed and pressure deficit also reveal the major intensification of NST B. After 2080 s, surface winds reach and maintain F1 intensity for a 6-min span with a maximum speed of 39 m s^{-1} occurring at 2300 s. The peak pressure deficit of 7.1 mb occurs just 20 s before the occurrence of maximum wind speed. The signal of NST B's demise (stage VI) emerges just as abruptly in the pressure and maximum wind time series, as was indicated in the time–height cross sections for vertical vorticity and vertical velocity seen in Fig. 13. There appears to be a vertical continuity in the collapse of NST B, indicating a strong connection between processes taking place both in cloud and near the surface. This connection is the downdraft prevalence aloft and related negatively buoyant outflow near the surface. Both pressure deficit and maximum wind speed continue dropping rapidly until the simulation's end. Through the period starting with the beginning of stage IV and ending within stage VI, NST B maintained maximum surface winds of greater than 30 m s^{-1} for an 11-min period. Along with the analyzed evolution of the NST family presented in section 3, the time–height cross sections and time series have provided a means by which the developmental stages of the NST family could be delineated using measures of misocyclone, NST, and storm strength and by employing intervariable comparison to infer changes within the NST storm system that drive these life cycle stages.

b. Vorticity redistribution, maintenance, and intensification

As noted in the previous sections, a key tenet of the observational model of NSTG included a vorticity pool that originated at low levels and built vertically in conjunction with developing deep convection overhead. This upward redistribution of vertical vorticity, apparent in radar observations of deep circulations associated with some NSTs (Wilson 1986; WW89; RW95), can be evaluated by assessing the vertical advection of vertical vorticity. The vertical vorticity tendency equation can be written as

$$\frac{\partial \zeta}{\partial t} = -\mathbf{V}\cdot\nabla\zeta + \boldsymbol{\omega}_h\cdot\nabla w + \zeta\frac{\partial w}{\partial z}, \tag{4}$$

where the right-hand side terms represent the advection

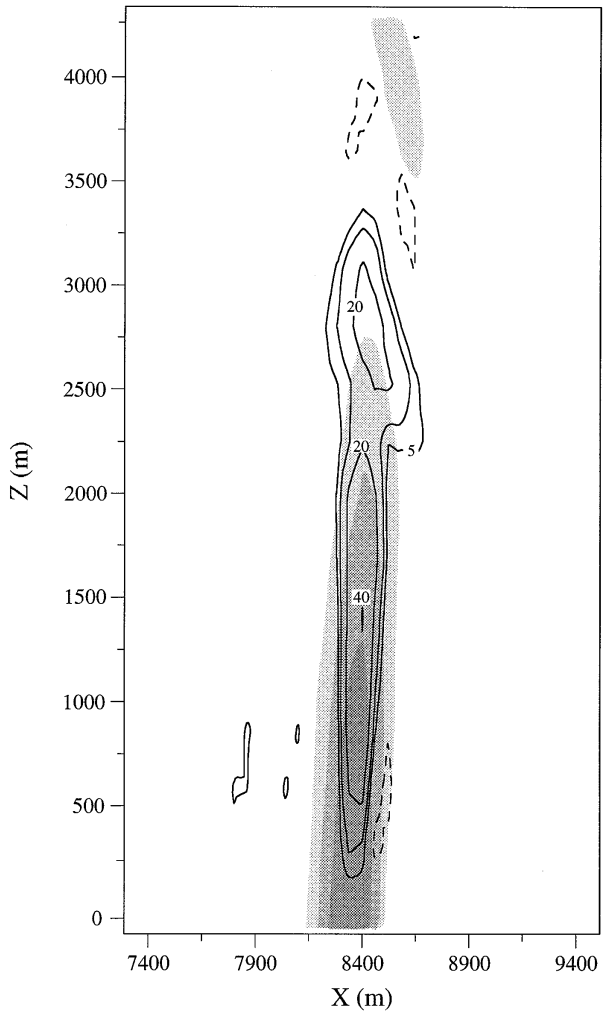

FIG. 16. Vertical X–Z cross section at 1440 s of gray-shaded vertical vorticity and contoured vertical advection of vertical vorticity associated with the second misocyclone from the north boundary seen in Fig. 4. The advection contour intervals displayed are −10, 5, 10, 20, and 40 × 10^{-4} s^{-2}. The gray-shaded regions correspond to vertical vorticity greater than 0.04 (light gray), 0.1 (medium gray), and 0.2 s^{-1} (dark gray).

of vertical vorticity (ζ), the tilting of horizontal vorticity ($\boldsymbol{\omega}_h$), and the stretching of vertical vorticity, respectively. The advection term may be further subdivided into horizontal and vertical components, the latter of which,

$$\left(\frac{\partial \zeta}{\partial t}\right)_{\mathrm{ADV}_z} = -w\frac{\partial \zeta}{\partial z}, \tag{5}$$

was used to analyze the vertical development of the misocyclone circulations of this modeling study. Shown in Fig. 16 is an *X–Z* slice of vertical vorticity and vertical advection of vertical vorticity for the second misocyclone from the north boundary shown in Fig. 4 at 1440 s. A clear pattern of vertical transport of ζ is present, with large advection values exceeding 10 × 10^{-4} s^{-2} through a deep column extending to the 3.5-km level. At these advection rates, only 100 s would be required for a particular level within this column to realize a ζ increase of 0.1 s^{-1}. The stretching and tilting terms in this column above 1.5 km are generally less then 30% of the magnitude of the vertical advection term; thus, the deep vorticity distribution seen in the time–height profile of Fig. 13a is accounted for mainly through vertical transport. The combined misocyclone and moist convective updraft acts as a vorticity pump to transport vertical vorticity from near the surface well into the storm's midlevels. This process explains the onset of visible rotation present in animations of the model cloud field associated with the simulated misocyclones and may explain similar observational phenomena.

Analysis of the vortex dynamics operative along outflow boundaries possessing leading edge vertical vortex sheets as described in detail in LW97 and as summarized in section 3a have established how large pools of vorticity on the misocyclone scale (1–2 km in diameter) can be established over relatively short timescales (~15–20 min). Short-lived tornado events of several minutes' duration could be explained through the contraction (stretching) of these misocyclone-scale vorticity pools; however, many observed NST events as well as the NST family simulated here have life spans exceeding 10 min. Other mechanisms supplying vertical vorticity to the low-level tornadic region must be operative to maintain these vortices. Two mechanisms have been identified in these NST simulations. The primary mechanism involves the northward transport of vertical vorticity along the outflow boundary to NST B as shown in Fig. 17 for 2060 s. Vertical vorticity magnitudes exceeding 0.04 s^{-1} have become reestablished along a vortex sheet, which extends south along the occlusion boundary and the north–south branch of the outflow boundary. A slightly weaker vortex sheet has also developed along the west–east branch of the outflow. The vortex-relative flow regime along these sheets supports the net transport of vertical vorticity toward the southeastern periphery of NST B. To examine the vorticity evolution for parcels entering the NST circulation from the vortex sheet, time-dependent trajectory analysis was performed. This analysis revealed that parcels entering the tornado periphery at z = 20 m, with a vertical vorticity of 0.04 s^{-1}, experienced a dramatic increase in vertical vorticity to 0.26 s^{-1} in just one-half revolution (30 s), while ascending to 135 m. This increase in vorticity was nearly entirely due to stretching. When parcels enter the vortex periphery, they encounter convergence of 0.061 s^{-1} averaged through a depth of 135 m. The stretching spinup time may be found by considering just the stretching portion of the vorticity tendency equation [Eq. (4)] and integrating with respect to t and ζ. Using the reported values of convergence and the initial vertical vorticity, only a 30-s spinup time is required for these parcels to attain vertical vorticity of 0.25 s^{-1}.

A secondary mechanism supplying vertical vorticity

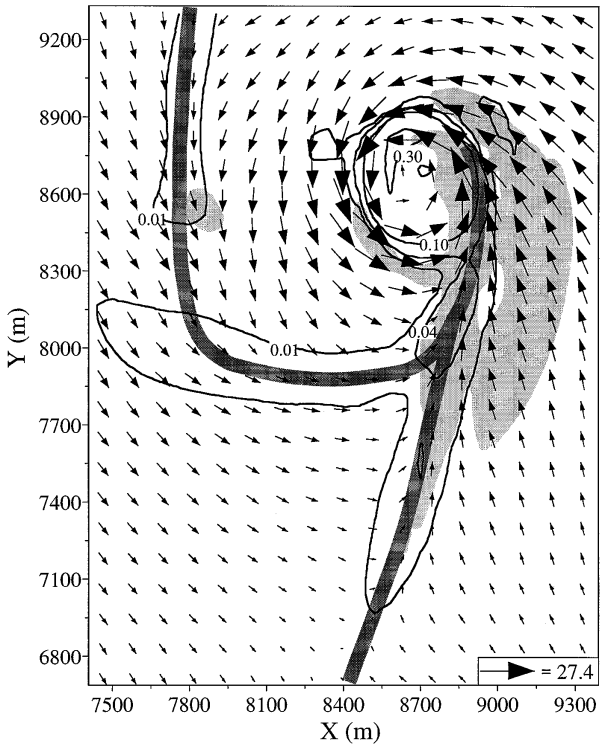

FIG. 17. Horizontal cross section of contoured surface vertical vorticity, NST-relative surface wind, and 40-m positive vorticity tendency tilting term (shaded) in the region near NST B at 2060 s. For reference, the surface outflow boundary position is delineated by the dark gray line. The vertical vorticity contours shown are 0.01, 0.04, 0.10, and 0.3 s^{-1}. Maximum velocity vector (m s^{-1}) is shown in the lower right corner. The gray-shaded region designates the area where the tilting term is greater than 1.0×10^{-4} s^{-2}.

to NST B involves the tilting of horizontal vorticity in the low-level ($z < 100$ m) inflow region east and southeast of NST B, as shown in Fig. 17. Parcels entering NST B from this region subsequently undergo stretching as they experience convergence along the vortex periphery. The horizontal vorticity present in this inflow region results from vertical shear caused by surface friction. An axis of maximum horizontal vorticity becomes established along the leading edge of the outflow boundary where ambient air is entrained under the friction induced outflow ''nose.'' Tilting of this horizontal vorticity occurs along the east–west updraft gradient seen in Figs. 6 and 10. Although positive tilting term values in this region are only in the range 1×10^{-4} to 7×10^{-4} s^{-2}, this mechanism provides a modest vertical vorticity contribution over short periods. Time-dependent trajectories and analysis of the tilting and stretching mechanisms were used to evaluate the vorticity evolution of parcels passing through this region of positive tilting and subsequently into NST B during the period 2000–2110 s. Parcels entering this region of positive tilting from the southeast at the 25-m level have residence times of about 50 s before encountering the NST's ring of strong peripheral convergence. During these 50 s, the parcels experience positive tilting of $\sim 2 \times 10^{-4}$ s^{-2}, which would result in the generation of vertical vorticity of 0.01 s^{-1}. The parcels then enter the vortex periphery, where, over the next 60 s, the parcels rise rapidly within the NST's updraft annulus to the $z =$ 480-m level. During this ascent, the parcels experience layer average convergence of 0.038 s^{-1}, which, considering only vortex stretching, would result in an increase in vertical vorticity to 0.1 s^{-1}.

To examine how the primary intensification mechanisms change from the NST early mature stage to the NST late mature stage with respect to ongoing storm processes, the stretching and tilting terms of the vorticity tendency equation [Eq. (4)] are utilized. Shown in Fig. 18 for representative vortex NST B are contour plots of the stretching term at the 60-m level for times 1860 and 2200 s. At 1860 s, positive vortex stretching at values greater than 10×10^{-4} s^{-2} occurs over the majority of the vortex region with values greater than 100×10^{-4} s^{-2} realized in a small area in the northeast quadrant. The region of negative stretching is associated with the axial downdraft seen in Fig. 6. Positive tilting at this level and time (not shown) is similar in configuration to the area of positive tilting shown in Fig. 17 (for 2060 s) and is generally more than an order of magnitude weaker than the stretching term. Examination of higher levels in the boundary layer revealed no regions of significantly larger positive tilting near the NSTs.

With the advent of new cold pools emerging into the low-level flow field at approximately 2000 s, the pattern and magnitude of the stretching term by 2200 s changes substantially along with the vortex diameter (Fig. 18). In response to the increasing convergence along the periphery of the NST circulations from the expanding cold pools, a pattern of strong vortex stretching at 60 m completely encircles the low-level vortex, with a large embedded area of stretching values greater than 100×10^{-4} s^{-2} covering most of the northeast half of the vortex. To put this value in perspective, only 40 s would be required to realize tornadic level vorticity values (~ 0.4 s^{-1}). In fact, an area of very strong stretching emerges along the north side of NST B, with a peak value well above 200×10^{-4} s^{-2}. Stretching term values are 2–5 times larger than those observed at 1860 s over all but the very center of the tornadic circulation. This signal of increased low-level vorticity stretching is documented in a time–height cross section of peak vortex stretching values compiled for the region associated with NST B's circulation, as shown in Fig. 19. Not only do the stretching values increase markedly after 2000 s but the depth of very strong stretching increases from the stage IV frictionally driven surface inflow layer depth of approximately 100 m to a depth of 300–400 m. Consistent with the time-series data presented in section 4a, a sharp drop in peak stretching magnitudes occur after 2360 s, spelling the decline of NST B. The core minimum in stretching seen in Fig. 18 at 2200 s is tied to the presence of axial downdraft penetrating to

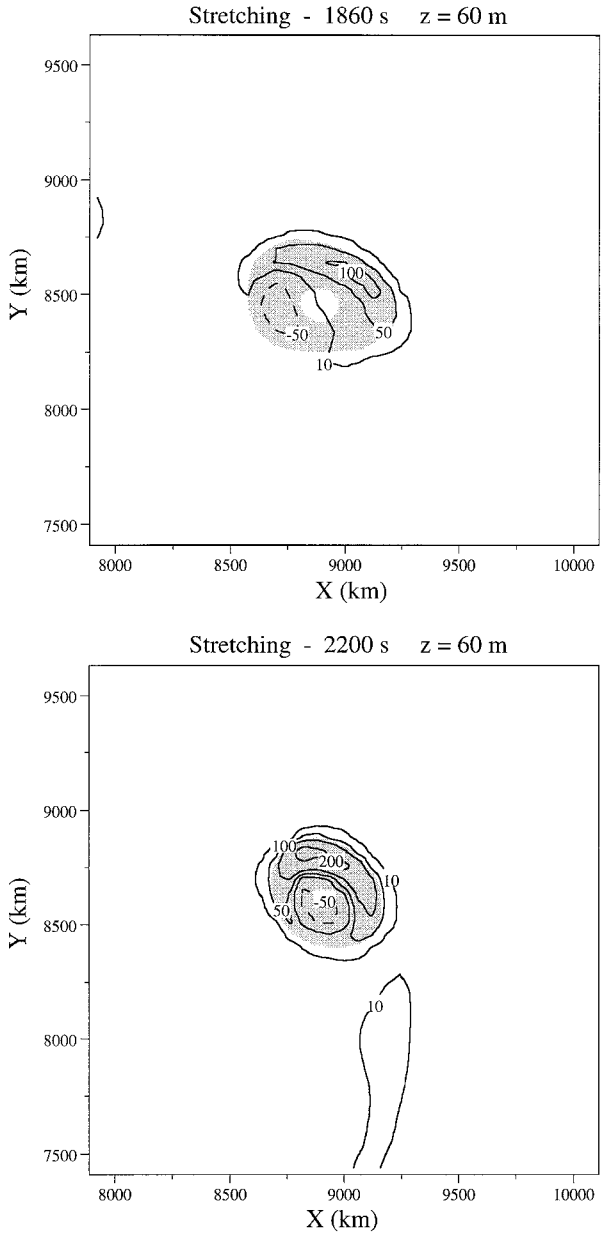

FIG. 18. Horizontal cross section of contoured vorticity tendency stretching term at 1860 and 2200 s at the 60-m level for the region near NST B. For reference, the background gray-shaded region designates areas with vertical vorticity greater than 0.1 s^{-1}. The stretching term contours shown are -50, 10, 50, 100, and 200 $\times$ 10^{-4} s^{-2}.

near the surface (Fig. 11). Positive tilting at 60 m (not shown) takes on a ringlike configuration on the periphery of NST B and remains generally more than an order of magnitude smaller than the stretching term at 2200 s.

The tilting term was examined at higher levels in the boundary layer at 2200 s to see if the introduction of new cold pools into the local NST environment would prompt much larger positive tilting term contributions. The notion here is that, with the emergence of a number of strong thermal boundaries as shown in Fig. 9, large

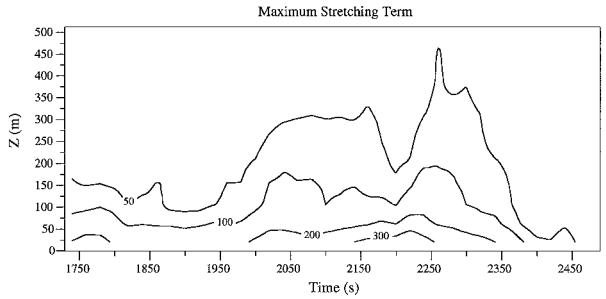

FIG. 19. Time–height cross section of peak vorticity tendency stretching term values associated with NST B. The stretching term contours shown are 50, 100, 200, and 300 $\times$ 10^{-4} s^{-2}.

values of baroclinically generated horizontal vorticity should arise along the leading edges of these expanding pools. Note that by 2200 s some of the new cold pools have surface maximum potential temperature deficits at their center of -8 K. Featured in Fig. 20 is the horizontal vorticity vector field and tilting term for the region near NST B at the 500-m level. As expected, the environment surrounding NST B has become rich in narrow bands of horizontal vorticity aligned along the leading edges of the cold pools. The large horizontal vorticity vectors observed within the tornadic circulation proper are at-

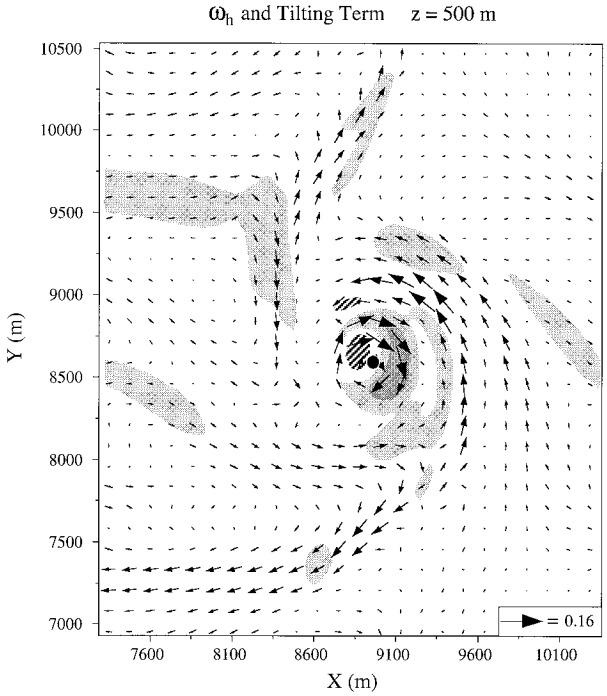

FIG. 20. Horizontal vorticity ($\boldsymbol{\omega}_h$) vectors and shaded regions of vorticity tendency tilting term at 2200 s for NST B at the 500-m level. The maximum horizontal vorticity vector magnitude (s^{-1}) is shown in the lower right corner. The light and dark gray shading represents regions where tilting term magnitudes exceed 1 $\times$ 10^{-4} and 10 $\times$ 10^{-4} s^{-2}, respectively. The hatched area represents negative tilting of magnitudes less than -10 $\times$ 10^{-4} s^{-2}. The black dot represents the center of circulation.

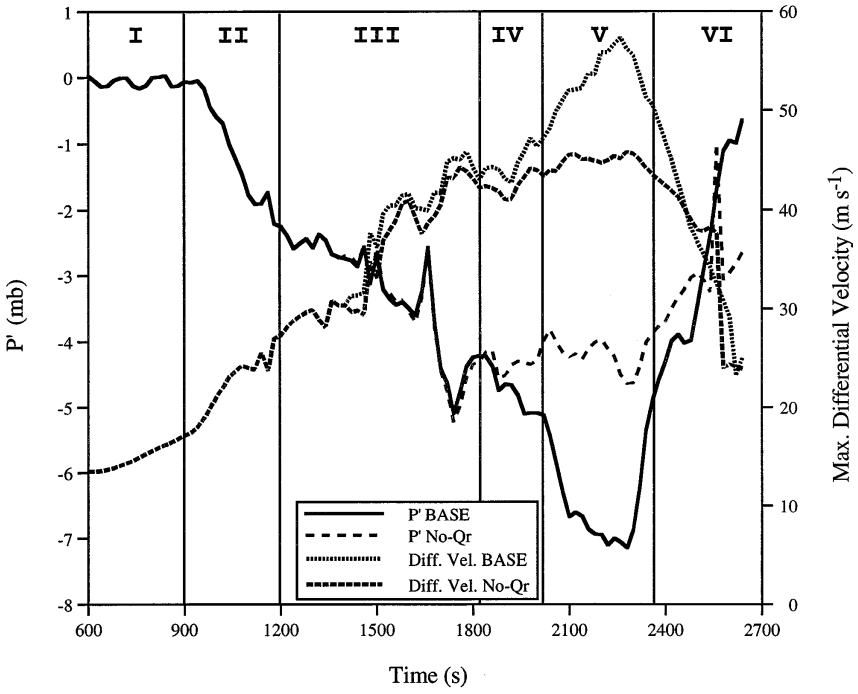

FIG. 21. Time series of maximum surface pressure deficit (with respect to the local surrounding environment) and maximum surface across-vortex differential velocity for the evolution of NST B in the BASE and No-Qr simulations. The BASE life cycle stages are overlaid on these time series.

tributed to the very large horizontal gradient in vertical velocity associated with NST B's updraft annulus. There are no organized regions of strong tilting that might be associated with the ingestion of baroclinically generated streamwise vorticity into the NST B circulation. The only regions of modest tilting at 500 m are inside the tornadic circulation and are artifacts of the vertically tilted orientation of the vortex tube at this level. A similar tilting term analysis was undertaken at higher levels in the boundary layer with comparable results.

This analysis has highlighted the primary role stretching plays in low-level vortex intensification and further accentuates the role played by the new outflows. In stage V, the combination of surface-friction-induced convergence into NST B and outflow-produced convergence around NST B leads to very strong low-level vortex intensification through stretching. As discussed in section 3b, concurrently occurring moist convection above these circulations is providing a positive feedback by inducing local convergence in the subcloud layer, which, in concert with the low-level convergence mechanisms just addressed, supports a strong and tall vortex along with a deep updraft annulus that couples the surface with the storm midlevels as shown in Fig. 11. The mature vortices are primarily maintained by vertical vorticity transported into the tornado circulations from a vortex sheet along the outflow boundary. A secondary maintenance mechanism involved the inflow of vertical vorticity produced from the tilting of horizontal vorticity southeast of the NSTs. No strong signal of vertical tilting of baroclinically generated horizontal vorticity was indicated, even after convective downdraft associated new outflow pools emerged in the environment surrounding the misocyclones.

5. Assessing the impact of new outflow and deep moist convection

a. Comparative No-Qr simulation

To examine the degree of influence that the emergence of new outflow pools have on NST intensity and longevity, the model was rerun with all parameters set as they were for the BASE simulation with the exception that the production of rainwater was turned off in MSTFLOW. The lack of rainwater precipitation in this simulation eliminates the creation of subcloud layer storm outflow from evaporation and water loading. By comparing some intensity measures for NST B between this simulation designated No-Qr and BASE, a quantitative assessment of the new outflow's impact on NST intensification may be made.

Time series of the maximum surface pressure deficit and the maximum surface across-vortex differential velocity shown in Fig. 21 were created in a similar manner to that discussed in section 4a for the development and evolution of NST B in the No-Qr and BASE simulations. The pressure and wind traces lie nearly on top of each

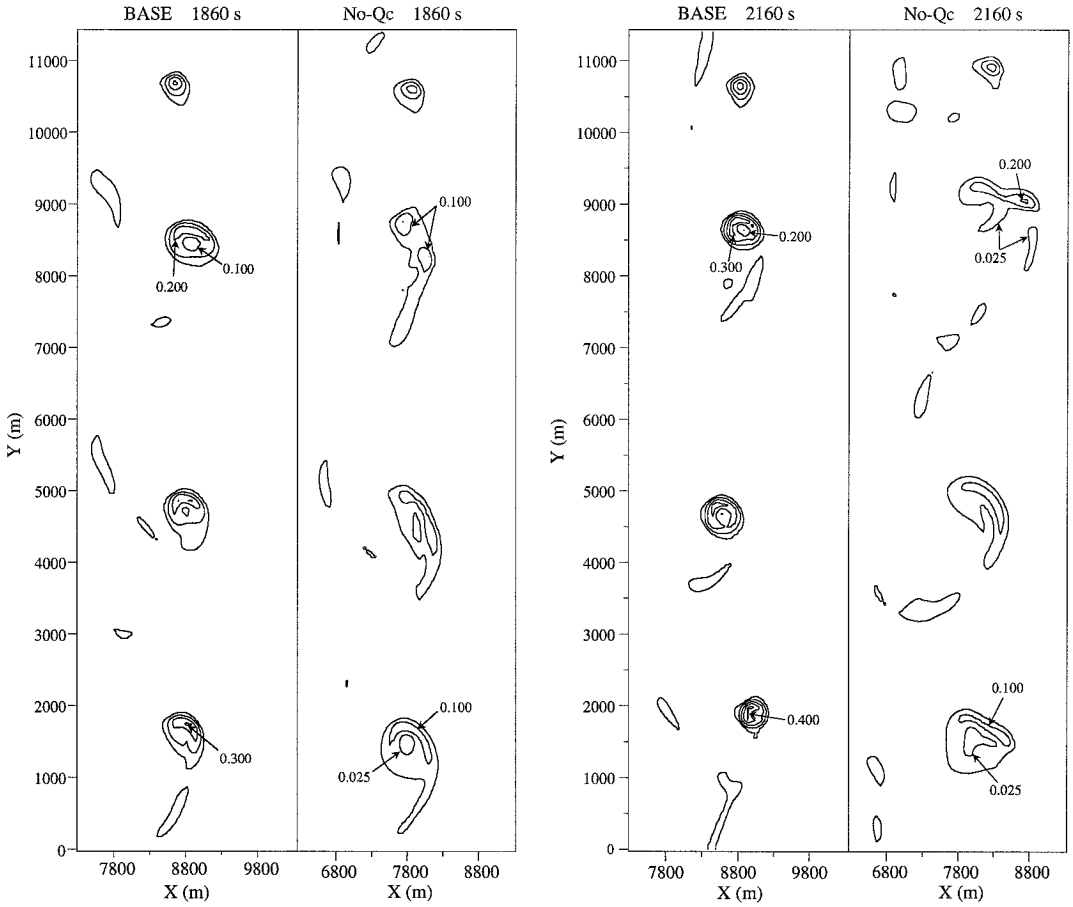

FIG. 22. Outflow leading edge surface vertical vorticity configuration for BASE and No-Qc at times 1860 and 2160 s. Vertical vorticity contour intervals used are 0.025, 0.1, 0.2, 0.3, and 0.4 s^{-1}.

other through the first three stages as anticipated, given that the big difference between these runs lies with the outflow–NST interaction. After a slight divergence in NST intensity by both indicators in stage IV, a pronounced signal of outflow induced intensification is observed in stage V for BASE. BASE simulation peak differential velocity is 25% higher than No-Qr and peak pressure deficit is 53% higher than No-Qr. A comparison of peak vertical vorticity observed over the most intense 2-min period in stage V (not shown) reveals a nearly 25% increase in vertical vorticity for BASE versus the No-Qr simulation. A similar pattern of outflow-induced intensification is observed for the other two major vortices NST C and NST D. In essence, the No-Qr simulation does not have a stage V, rather an extended stage IV that lasts approximately 9 min before dissipation begins. The No-Qr simulation may represent observed cases where storm outflow is very weak, allowing the tornado to persist for an extended period at quasi-steady intensity. These cases may, in general, be inherently weaker due to the absence of outflow-induced low-level vortex stretching. For instance, surface winds for NST B in the No-Qr simulation only briefly reached low F1 intensity and mainly were in the high F0 range. As shown in Fig. 21, the pressure deficit and differential velocity for NST B in the No-Qr case begins a much more moderate decline in intensity after 2300 s than observed for BASE, due to the absence of new strong outflow into the subcloud layer. The demise of the NSTs in No-Qr occurs as the low-level circulations gradually become wrapped in stable air from within the original weak outflow. Vortex intensification through stretching is inhibited and the vortex maintenance mechanisms described in section 4b no longer support the NSTs.

b. Comparative No-Qc simulation

To assess the organizational impact and intensification properties of deep moist convection above the evolving outflow leading edge vortices, a simulation designated No-Qc was completed in which the cloud microphysics were turned off in MSTFLOW. With no deep moist convection present over the evolving line of vortices, a much different evolution of leading edge circulations occurred. The vertical vorticity contour plots shown in Fig. 22 display a comparison of the

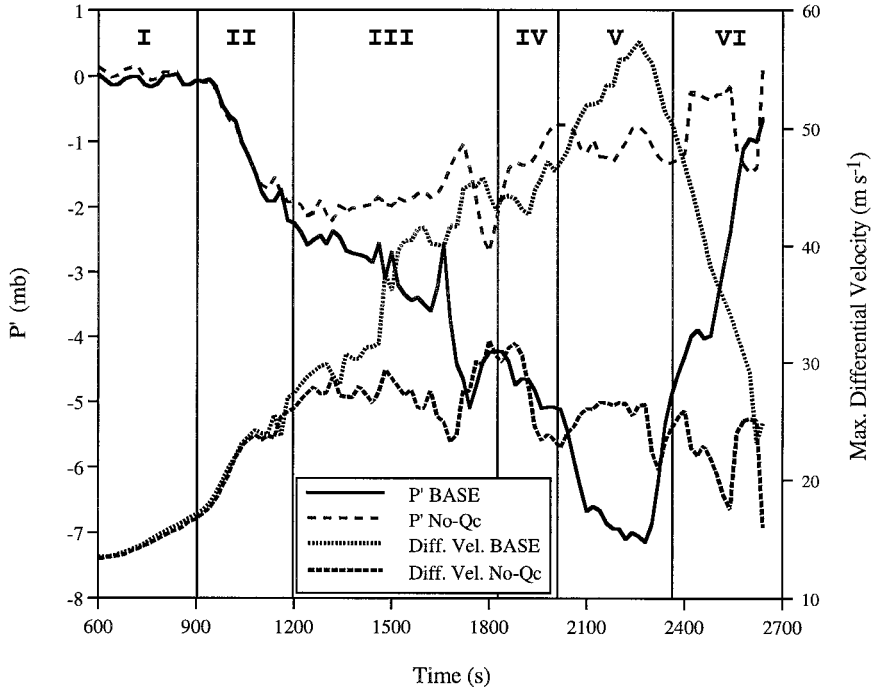

FIG. 23. Time series of maximum surface pressure deficit (with respect to the local surrounding environment) and maximum surface across-vortex differential velocity for the evolution of NST B in BASE and NST B's counterpart circulation in No-Qc. The BASE life cycle stages are overlaid on these time series.

configuration of leading edge vortices for BASE and No-Qc at two times, 1860 and 2160 s. In both runs the pools of vorticity by 1860 s are positioned at similar locations along the outflow leading edge; however, structurally the No-Qc vortex pools are much larger in physical dimension and lack a uniform quasi-circular shape as in BASE. In association with this larger physical size, the vertical vorticity magnitudes are much smaller in No-Qc at 1860 s. At 2160 s, the BASE NSTs have narrowed further and intensified, while the No-Qc circulations have remained approximately steady in strength while maintaining a loose integrity. Comparative differences in characteristics such as larger size, elongated shape, and weak vorticity magnitudes are indicative that the boundary layer environment in No-Qc lacked the convergence and resultant stretching supplied by the deep moist convection present in BASE.

To obtain a more quantitative assessment of the intensity difference between the developing NST B circulation and its counterpart in No-Qc, time series of peak pressure deficit and maximum across-vortex differential velocity are presented in Fig. 23. Nearly identical series for both indicators are seen up through the vortex sheet roll-up process of stage II. Coincident with the strong updraft pulse of rapidly developing moist convection indicated in Fig. 13b, the pressure deficit and differential velocity traces between BASE and No-Qc begin a divergent trend at approximately 1200 s that continues until late in stage V of BASE. The time of maximum intensity (for the indicators used here) for NST B's counterpart circulation in No-Qc occurs much earlier than BASE at a time near 1800 s with a peak pressure deficit of 2.7 mb and differential velocity of 32 m s^{-1}. For comparison, NST B in BASE reaches maximum intensity near 2260 s with a peak pressure deficit of 7.1 mb and maximum differential velocity of 57 m s^{-1}. A trend toward general weakening of these intensity indicators after 1800 s in No-Qc continues until the end of the simulation. No tornadic intensity vortices ever develop in No-Qc. It is readily apparent in this time series that the moist convection aloft begins to have an impact on the misocyclones quite early in the NSTG process. This impact becomes increasingly magnified even before ancillary storm processes produce new outflow that sharply intensify the BASE NSTs after 2000 s. These comparative time series provide further evidence of the important role that overhead rapidly developing moist convection plays in providing the proper convergent subcloud environment for NSTG to commence.

6. Summary and discussion

In conjunction with Part I of this article series, which examined the development of pretornadic misocyclones along an outflow boundary, a comprehensive morphology of the development of simulated NSTs along convergence lines such as thunderstorm outflow boundaries

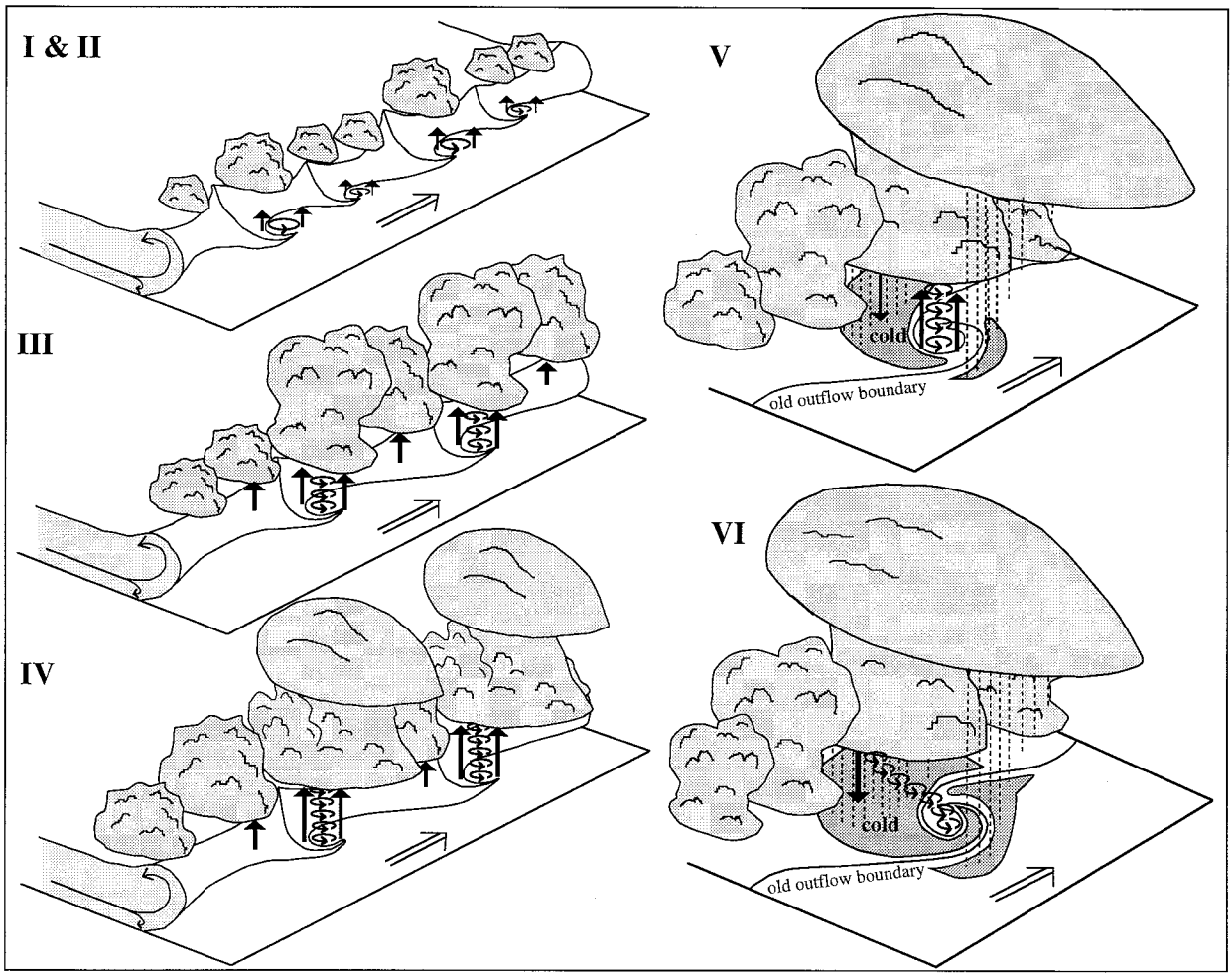

FIG. 24. Schematic presentation of the life cycle stages of NST evolution. The diagrams for stages V and VI focus in on just one member of the NST family. The viewing perspective is from an elevated position looking northwest. See text for details.

has been documented. Through an identification of the ongoing processes integral to each life cycle stage of NST development and dissipation, a ''refined'' model of NSTG and decay that builds on the current observational model outlined in WW89 and BS89 (with added detail in RW95) has been created. To illustrate the refined model, a schematic presentation of the life cycle stages of NST evolution is provided in Fig. 24. Nonsupercell tornadogenesis along outflow boundaries appears highly dependent upon the vortex sheet dynamics operative along the outflow leading edge. The vortex sheet development stage (I) commences as an outflow boundary (or other convergence boundary) encounters an air mass with a low-level wind field possessing a component of motion directed parallel to the outflow leading edge. This interaction of air masses creates a narrow transition zone of marked horizontal shear (i.e., a vertical vortex sheet) aligned along the leading edge of the boundary. Horizontal shearing instability is triggered along this vortex sheet by perturbations present at the outflow leading edge. Lobe and cleft instability provides a source for these triggers, although other possible triggers may include, but are not limited to, horizontal convective roll intersections with the outflow boundary, natural variations in the surface roughness, or naturally occurring variations in the outflow thermal field. As the horizontal shearing instabilities develop, the vortex sheet rolls up along with the outflow leading edge in the vortex sheet roll-up stage (II). Once the bulk of the vertical vorticity along the sheet has been effectively concentrated in the maturing horizontal shearing instabilities (i.e., first generation misocyclones) by preferential vorticity advection induced by the instabilities, interaction between vortices soon follows in the misocyclone interaction and merger stage (III). The two common interactions include vortex pairing events, where vortices of similar strength pair off and ultimately coalesce, and vorticity extrusion events, whereby a stronger vortex extrudes (or mines) the vorticity from its weaker neighbor(s). These vortex interactions produce a longer wavelength misocyclone pattern that contains larger circulations that may then be subject to strong

vortex stretching. These larger misocyclones produce an asymmetric pattern of moist convective forcing along the outflow leading edge. The deep convection that forms above the misocyclones is supported by air parcels originating near the surface that are carried aloft to their level of free convection by updrafts driven both by the low-level misocyclone and by the subcloud layer convergence induced by the moist convection. As the young storms rapidly develop, vertical vorticity is redistributed from the boundary layer to the storm midlevels through vertical advection by the coupled misocyclone and storm updraft. The NST early mature stage (IV) occurs as low-level stretching, due primarily to surface-friction-induced inflow, intensifies the misocyclone circulations to tornadic intensity. Concurrently, moist convection occurring above these circulations further supports NST intensification by inducing subcloud convergence and weak vortex stretching throughout the depth of the boundary layer. The mature vortices are primarily maintained by vertical vorticity transported at levels near the surface into the tornado circulation from a vortex sheet along the outflow boundary. A secondary maintenance mechanism involved the inflow of vertical vorticity produced from the tilting of low-level horizontal vorticity southeast of the NSTs. The most intense phase, the NST late mature stage (V), occurs concurrent with the emergence of new precipitation-induced cold pools that bound the NST, increasing the low-level convergence and significantly increasing the associated vortex stretching on the periphery of the NSTs. In stage V, the diameter of the NSTs decrease substantially in response to outflow-induced peripheral convergence. The transition to a predominant downdraft character for the storm complex and negatively buoyant subcloud air mass heralds the onset of the NST dissipation stage (VI). The NSTs tilt sharply when their lower portions are advected along with the strongest nearby advancing cold pool, creating a roping out appearance. Cold negatively buoyant downdraft air quickly surrounds and becomes entrained into the low-level circulations, leaving a good portion of the vortex in descending and divergent motion, ultimately dissipating the tornado. Although a weak outflow boundary was used here, this refined model should be generally applicable to other boundaries possessing marked horizontal shear commonly associated with NSTs. The scenarios for NSTG and decay along differing boundaries may vary in the type and spacing of the initial perturbations that trigger horizontal shearing instability growth along the vortex sheet.

In general, the main points of the observational model of WW89 and BS89 are largely confirmed by this numerical study, including 1) the presence of shearing instability, which created the misocyclones along a low-level convergence boundary; 2) the source of tornadic rotation originating near the surface; and 3) stretching as the primary means of vortex intensification as the misocyclone circulation comes under the influence of rapidly deepening overhead convection. Evidence of significant vertical tilting of baroclinically generated horizontal vorticity was not observed in this simulation even after the introduction of markedly baroclinic new cold pools. Results presented here and in LW97 suggest that the locational relationship between the misocyclone and deep convection may not simply be a matter of fortune, but rather that the misocyclones influence the pattern of convective forcing along the outflow boundary. An in-depth numerical study of the influence of misocyclone circulations on deep moist convection is currently under way by the authors. An alternative suggestion for the forcing that controls the pattern of deep convection observed along convergence boundaries involves the positioning of boundary layer horizontal convective roll intersections with the primary convergence line (Wilson et al. 1992; Wakimoto and Atkins 1994). The actual mechanism responsible for observed patterns of initial deep convection is likely highly situation dependent. Whatever the controlling factors are for moist convective forcing, when no moist convection existed overhead, the resultant misocyclones acutely lacked the coherent organization and intensity of the misocyclones and NSTs of BASE.

The concept of a family of tornadoes as simulated may initially appear to be a highly anomalous event. Observational evidence and modeling studies such as this one would argue, given the paradigm of a vortex sheet breaking down into a number of candidate vortices, that under the proper vertical shear and deep convective thermodynamic environment, a number of simultaneously occurring NSTs are possible. Viewed in this context, it is not surprising that when one NST is observed it is not unusual to see others occurring nearly simultaneously along a developing line of storms associated with a common boundary. This family aspect also likely applies to generally weaker vortices such as gustnadoes (Doswell 1985) observed along the leading edge of outflow boundaries that possess significant across-front horizontal shear (such as the forward- and rear-flank boundaries of supercell thunderstorms).

This modeling study has identified a major role for new storm outflow in NST intensification. Previous modeling work (Lee 1994) had suggested that new outflow played a role in NST intensification. The observational NST study by RW95 showed that, while the presence of new storm outflow was not a prerequisite to tornadogenesis, consistent with the stage IV NSTs simulated here, new outflow may play a role in the timing and intensity of NSTs. The vortex intensification analysis for this simulation and supporting observational evidence of RW95 indicate that as new outflow interacts with the low-level portions of the tornado it dramatically increases the local convergence and resultant vortex stretching. Comparative results using a simulation without the rain production microphysics turned on (eliminating the generation of new cold storm outflow) indicated that the outflow interaction markedly increased the NST intensity as indicated by a 25% in-

crease in across-vortex differential velocity and vorticity and corresponding 53% larger pressure deficit.

The ''refined'' model of NST evolution presented above may be, in part, applicable to other tornadic vortex types as well. For instance, in some tornadoes that challenge current classification schemes such as the strong (F3) Newcastle, Texas, tornado of 29 May 1994, documented in the radar analysis of Wakimoto and Atkins (1996), tornadogenesis occurred in conjunction with a low-level shear feature that deepened and intensified coincident with rapidly deepening convection along the flanking line of a supercell thunderstorm well away from the mesocyclone location. It appears that the vortex intensification stage is broadly similar to that presented here, although how the large pool of vorticity at low levels originated is uncertain. How similar are some of the stages outlined in the ''refined'' model to the morphology of developing incipient low-level vertical vorticity zones near the tornadic region of supercell thunderstorms? Brandes (1977, 1978) has suggested the possibility that vertical vorticity may be concentrated in a manner whereby a vortex sheet residing in the vicinity of a supercell's mesocyclone rolls up to form circulations potentially important to tornadogenesis, a process not unlike stage II of the schematic model of NSTG.

The tornadogenesis model also appears to share much in common with waterspout formation. In Golden's (1974a, b) observational studies of waterspouts in the 1970s, a detailed morphology of waterspout development was compiled that shares several aspects of the refined model. Golden suggested that multiple dark spots observed on the sea surface represented waterspout embryo circulations that were created from shearing instabilities forming along a vertical vortex sheet. This may be analogous to the first evolution horizontal shearing instabilities simulated in this study. Dark spots forming in close proximity were not observed to persist individually, indicating that vortex mergers were also occurring in some cases, similar to stage (III). In waterspout cases, the intensification and decay of the vortices were associated with respective periods of updraft growth and decay in the convective cloud line, similar to the scenario for misocyclone–NST intensification and dissipation as presented here (stages III, IV, and VI). On a qualitative level, the three-dimensional images of the young NSTs shown in Fig. 4, positioned at the center of the wave spirals seen in the surface thermal field, appear strikingly similar in orientation to aerial photographs of waterspouts with respect to sea surface indications of similar shear–convergence boundaries (Golden 1974a). As close as the NSTG model may appear to partially explaining waterspouts, there is disagreement on the vertical vorticity source region in *some* waterspout events. Based on observational and modeling evidence, Simpson et al. (1991) argue for an in-cloud cumulus-scale source region of vertical vorticity for certain waterspout events, in clear contrast to the boundary layer vorticity source region of the NSTG model. Other significant contrasts exist between the environments of NSTs and waterspouts, which may include factors such as CAPE and surface roughness. Further high-resolution modeling studies are planned to investigate waterspout genesis.

Trial experiments leading up to the successful BASE simulation indicated a large sensitivity in the prerequisite conditions for producing a successful NST simulation that may, in part, explain why NST occurrence is not commonplace. This NSTG process appeared quite sensitive to the ambient vertical shear profile that would just balance the cold pool circulation to yield upright outflow leading edge structure and deep convection *directly* over the misocyclones. The NSTG process was also highly sensitive to the timing of rapid deep convective development. For instance, if the misocyclone interaction and merger stage (III) was not complete before storm maturity, the resulting NSTs were relatively weak. To further understand the sensitivities of the NSTG process, a series of parameter tests to be presented in Part III of this article series will explore the sensitivity of tornadogenesis to changes in initial vortex sheet strength, CAPE, and vertical shear. By understanding these sensitivities, the nowcasting community in NST-prone locations may greatly benefit.

Acknowledgments. The authors wish to thank Brian Jewett and Louis Wicker for many beneficial discussions on this topic. We also wish to recognize the visualization software development of Crystal Shaw and David Wojtowicz, which facilitated the analysis of these simulations. Rita Roberts and Jim Wilson of the National Center for Atmospheric Research provided data and valuable insight on the 15 June 1988 Denver tornado outbreak. Peter Blottman graciously provided slides and video documentation of the 4 June 1995 Lazbuddie, Texas, NST family. This research was supported by the National Science Foundation under NSF Grants ATM-92-14098 and ATM-96-33228 and by the National Center for Supercomputing Applications. These simulations were performed on the Connection Machine (CM-5) at the National Center for Supercomputing Applications. We gratefully acknowledge three anonymous reviewers whose suggestions helped improve this manuscript.

APPENDIX

Numerical Model Description

The MSTFLOW numerical model was created to simulate cloud and density current dynamics in a massively parallel computational environment. MSTFLOW is similar in design to the cloud model of Klemp and Wilhelmson (1978, hereafter KW78) and to the COMMAS cloud model described in Wicker and Wilhelmson (1995); however, the model code is written in CM FORTRAN, which allows computations to be done in a data-

parallel environment on the National Center for Supercomputing Application's Connection Machine. The model is a three-dimensional, nonhydrostatic, finite difference, convective cloud model that utilizes a quasi-compressible version of the Navier–Stokes equations. The Coriolis acceleration is ignored due to the high Rossby number of the flows being simulated. The momentum, thermodynamic, and pressure equations being solved can be written in Cartesian coordinates in the following form:

$$\frac{du_i}{dt} + c_p\overline{\theta}_v\frac{\partial \pi}{\partial x_i} = \delta_{i3}g\left[\frac{\theta}{\overline{\theta}} - 1 + 0.61(q_v - \overline{q}_v) - q_c - q_r\right] + D_{u_i}, \quad \text{(A1)}$$

$$\frac{d\phi}{dt} = M_\phi + D_\phi, \quad \text{(A2)}$$

$$\frac{\partial \pi}{\partial t} + \frac{c_s^2}{c_p\overline{\rho}\,\theta_v^2}\frac{\partial}{\partial x_j}(\overline{\rho}\overline{\theta}_v u_j) = f_\pi, \quad \text{(A3)}$$

where

$$f_\pi = -u_j\frac{\partial \pi}{\partial x_j} + \frac{R_d\pi}{c_v}\frac{\partial u_j}{\partial x_j} + \frac{c_s^2}{c_p\theta_v^2}\frac{d\theta_v}{dt} + D_\pi, \quad \text{(A4)}$$

and the substantial derivative is

$$\frac{d}{dt} = \frac{\partial}{\partial t} + u_j\frac{\partial}{\partial x_j}.$$

The nondimensional pressure and virtual potential temperature are defined as

$$\overline{\Pi} + \pi = \left(\frac{p}{p_0}\right)^{R_d/c_p} \quad \text{(A5)}$$

$$\theta_v = \theta(1 + 0.61q_v). \quad \text{(A6)}$$

In this equation set, u_i ($i = 1, 2, 3$) are the u, v, and w velocity components and π is the perturbation nondimensional pressure from the base-state value $\overline{\Pi}$. In Eq. (A2), ϕ represents the variables of potential temperature (θ) and the mixing ratio values for water vapor, cloud water, and rainwater (q_v, q_c, and q_r). Other variables and constants include the pressure (p), reference pressure ($p_0 = 1000$ mb), density (ρ), speed of sound (c_s), gravitational acceleration (g), gas constant for dry air (R_d), and specific heats of dry air at constant pressure (c_p) and constant volume (c_v). The variables with overbars are base-state values that are functions only of height. The M and D terms are contributions from cloud microphysics and from subgrid-scale mixing. The terms that make up f_π have been shown to be inconsequential to the physical processes of importance in the model and are thus ignored (KW78).

The moist microphysics formulation is based on three categories of water that include water vapor, cloud water, and rainwater. Rainwater quantities are assumed to exist in Marshall–Palmer drop distributions (Marshall and Palmer 1948) and have terminal fall speeds based on a mass-weighted formulation adjusted for atmospheric density variations. A cloud water threshold must be met before the autoconversion of cloud water to rainwater is allowed to take place. The threshold value selected ($a = 0.003$ g g^{-1}) is consistent with the comments of Soong (1974) for the continental nature of the clouds simulated. See Durran and Klemp (1983) for specific details of this cloud microphysics parameterization.

A diagnostic turbulent mixing parameterization similar to that designed by Clark (1979) is employed. The subgrid-scale momentum mixing term D_{u_i} in Eq. (A1) can be written as

$$D_{u_i} = \frac{\partial}{\partial x_j}(\tau_{ij}), \quad \text{(A7)}$$

where the Reynolds stress tensor is specified in terms of the stratification and shear, according to the formulation of Smagorinsky (1963) and Lilly (1962),

$$\tau_{ij} = K_m D_{ij}. \quad \text{(A8)}$$

The deformation tensor is given by

$$D_{ij} = \frac{\partial u_i}{\partial x_j} + \frac{\partial u_j}{\partial x_i} - \frac{2}{3}\delta_{ij}\frac{\partial u_k}{\partial x_k}, \quad \text{(A9)}$$

and the total deformation is represented as

$$\mathrm{Def}^2 = \frac{1}{2}(D_{11}^2 + D_{22}^2 + D_{33}^2) + D_{12}^2 + D_{13}^2 + D_{23}^2. \quad \text{(A10)}$$

The momentum eddy mixing coefficients employed in horizontal mixing ($K_{m_{xy}}$) and in vertical mixing (K_{m_z}) are given by

$$K_{m_{xy}} = (c_m^2 l_m \Delta z)\left[\max\left(\mathrm{Def}^2 - \frac{B}{Pr}, 0\right)\right]^{1/2}, \quad \text{(A11)}$$

$$K_{m_z} = (c_m^2 \Delta z^2)\left[\max\left(\mathrm{Def}^2 - \frac{B}{Pr}, 0\right)\right]^{1/2}, \quad \text{(A12)}$$

where $l_m = (\Delta x\Delta y\Delta z)^{1/3}$ and $c_m = 0.21$ following Deardorff (1971). This split form of the momentum eddy mixing coefficient compensates for the mixing length changes associated with a stretched grid implementation. The calculation of the buoyancy term (B) is accomplished using the formulation of KW78 as follows:

$$B = \begin{cases} \dfrac{g}{\overline{\theta}}\dfrac{\partial \theta}{\partial z}; & q_c \le 10^{-6} \\ gA\dfrac{\partial \theta_e}{\partial z} - g\left(\dfrac{\partial q_c}{\partial z} + \dfrac{\partial q_r}{\partial z}\right); & q_c > 10^{-6}, \end{cases} \quad \text{(A13)}$$

where the equivalent potential temperature (θ_e) and A are given as

$$\theta_e = \theta + \frac{L}{c_p\overline{\Pi}}q_v, \tag{A14}$$

$$A = \frac{1}{\overline{\theta}}\left(\frac{1 + \dfrac{1.61\varepsilon L q_v}{R_d T}}{1 + \dfrac{\varepsilon L^2 q_v}{c_p R_d T^2}}\right). \tag{A15}$$

In the equations above, L is the latent heat of vaporization and ε has a value of 0.622. The subgrid-scale scalar mixing term D_ϕ in Eq. (A2) may be written as

$$D_\phi \sim \frac{\partial}{\partial x_j}\left(K_h\frac{\partial \phi}{\partial x_j}\right), \tag{A16}$$

where K_h is the scalar eddy mixing coefficient that is related to K_m by the relation

$$K_h = \frac{K_m}{\mathrm{Pr}} \tag{A17}$$

and the eddy Prantl number (Pr) is set to ⅓ (Deardorff 1972).

MSTFLOW employs centered, second-order ''box method'' spatial differencing (Kurihara and Holloway 1967) for advection and second-order ''leapfrog'' time differencing to integrate the equation set forward. An Arakawa ''C-grid'' is utilized in the placement of the model-dependent variables. The model is time split for efficiency in a similar fashion to KW78 so that terms responsible for the soundwave part of the solution are solved at a smaller time step than the terms responsible for the advection, buoyancy, and subgrid-scale mixing. A Robert (1966) time smoother is applied to all model variables, except π, at the large time steps to prevent solution separation associated with leapfrog time integration schemes. A fourth-order filter is applied in the horizontal to the momentum and scalar variables to inhibit the growth of nonlinear instabilities and other spurious short wavelength modes. Small, second-order vertical background damping is also applied to these variables for the same reasons. The coefficient (alowk) for this background vertical diffusion is given as a function of the stretched vertical grid by

$$\mathrm{alowk} = 0.125\Delta z. \tag{A18}$$

Boundary conditions for this model are discussed in section 2.

REFERENCES

Batchelor, G. K., 1967: *An Introduction to Fluid Dynamics.* Cambridge University Press, 516 pp.

Bluestein, H. B., 1985: The formation of a ''landspout'' in a ''broken-line'' squall line in Oklahoma. Preprints, *14th Conf. on Severe Local Storms,* Indianapolis, IN, Amer. Meteor. Soc., 267–270.

Brady, R. H., and E. J. Szoke, 1989: A case study of non-mesocyclone tornado development in northeast Colorado: Similarities to waterspout formation. *Mon. Wea. Rev.,* **117,** 843–856.

Brandes, E. A., 1977: Gust front evolution and tornado genesis as viewed by Doppler radar. *J. Appl. Meteor.,* **16,** 333–338.

——, 1978: Mesocyclone evolution and tornadogenesis: Some observations. *Mon. Wea. Rev.,* **106,** 995–1011.

——, 1984: Vertical vorticity generation and mesocyclone sustenance in tornadic thunderstorms: The observational evidence. *Mon. Wea. Rev.,* **112,** 2253–2269.

Carbone, R. E., 1983: A severe frontal rainband. Part II: Tornado parent vortex circulation. *J. Atmos. Sci.,* **40,** 2639–2654.

Chen, C., 1995: Numerical simulations of gravity currents in uniform shear flows. *Mon. Wea. Rev.,* **123,** 3240–3253.

Clark, T. L., 1979: Numerical simulations with a three-dimensional cloud model: Lateral boundary condition experiments and multicellular severe storm simulations. *J. Atmos. Sci.,* **36,** 2191–2215.

Corcos, G. M., and F. S. Sherman, 1984: The mixing layer: Deterministic models of a turbulent flow. Part 1. Introduction and the two-dimensional flow. *J. Fluid Mech.,* **139,** 29–65.

Davies-Jones, R. P., 1986: Tornado dynamics. *Thunderstorm Morphology and Dynamics,* E. Kessler, Ed., 2d ed., University of Oklahoma Press, 197–236.

Deardorff, J. W., 1971: On the magnitude of the subgrid-scale eddy coefficient. *J. Comput. Phys.,* **7,** 120–133.

——, 1972: Numerical investigation of neutral and unstable planetary boundary layers. *J. Atmos. Sci.,* **29,** 91–115.

Doswell, C. A., III, 1985: The operational meteorology of convective weather. Vol. II: Storm scale analysis. NOAA Tech. Memo. ERL ESG-15, 240 pp. [NTIS PB 85 226959/XAB.]

Durran, D. R., and J. B. Klemp, 1983: A compressible model for the simulation of moist mountain waves. *Mon. Wea. Rev.,* **111,** 2341–2361.

Fujita, T. T., 1981: Tornadoes and downbursts in the context of generalized planetary scales. *J. Atmos. Sci.,* **38,** 1511–1534.

Golden, J. H., 1971: Waterspouts and tornadoes over south Florida. *Mon. Wea. Rev.,* **99,** 146–154.

——, 1974a: The life cycle of Florida Keys' waterspouts. *J. Appl. Meteor.,* **13,** 676–692.

——, 1974b: Scale-interaction implications for the waterspout life cycle. *J. Appl. Meteor.,* **13,** 693–709.

——, and M. E. Sabones, 1991: Tornadic waterspout formation near intersecting boundaries. Preprints, *25th Int. Conf. on Radar Meteorology,* Paris, France, Amer. Meteor. Soc., 420–423.

Kingsmill, D. E., 1995: Convection initiation associated with a seabreeze front, a gust front, and their collision. *Mon. Wea. Rev.,* **123,** 2913–2933.

Klemp, J. B., and R. B. Wilhelmson, 1978: The simulation of three-dimensional convective storm dynamics. *J. Atmos. Sci.,* **35,** 1070–1096.

Kurihara, Y., and J. Holloway, 1967: Numerical integration of a nine-level global primitive equation model formulated by the box method. *Mon. Wea. Rev.,* **95,** 509–530.

Lee, B. D., 1994: The numerical simulation of non-supercell tornadogenesis. Ph.D. dissertation, University of Illinois, 215 pp. [Available from Dept. of Atmospheric Sciences, University of Illinois at Urbana–Champaign, Urbana, IL 61801.]

——, and R. B. Wilhelmson, 1997: The numerical simulation of non-supercell tornadogenesis. Part I: Initiation and evolution of pretornadic misocyclone circulations along a dry outflow boundary. *J. Atmos. Sci.,* **54,** 32–60.

Lemon, L. R., and C. A. Doswell III, 1979: Severe thunderstorm evolution and mesocyclone structure as related to tornadogenesis. *Mon. Wea. Rev.,* **107,** 1184–1197.

Lewellen, W. S., 1993: Tornado vortex theory. *The Tornado: Its Structure, Dynamics, Prediction, and Hazards, Geophys. Monogr.,* No. 79, Amer. Geophys. Union, 19–39.

——, D. C. Lewellen, and R. I. Sykes, 1997: Large eddy simulation of a tornado's interaction with the surface. *J. Atmos. Sci.,* **54,** 581–605.

Lilly, D. K., 1962: On the numerical simulation of buoyant convection. *Tellus,* **14,** 168–172.

Mahoney, W. P., 1988: Gustfront characteristics and the kinematics associated with interacting thunderstorm outflows. *Mon. Wea. Rev.,* **116,** 1474–1491.

Marshall, J. S., and W. M. Palmer, 1948: The distribution of raindrops with size. *J. Meteor.,* **5,** 165–166.

McWilliams, J. C., 1984: The emergence of isolated coherent vortices in turbulent flow. *J. Fluid Mech.,* **146,** 21–43.

Mueller, C. K., and R. E. Carbone, 1987: Dynamics of a thunderstorm outflow. *J. Atmos. Sci.,* **44,** 1879–1898.

Rasmussen, E. N., and J. M. Straka, 1996: Mobile mesonet observations of tornadoes during VORTEX-95. Preprints, *18th Conf. on Severe Local Storms,* San Francisco, CA, Amer. Meteor. Soc., 1–5.

Riley, J. J., and R. W. Metcalfe, 1980: Direct numerical simulation of a perturbed turbulent mixing layer. *AIAA 18th Aerospace Meeting,* Pasadena, CA, American Institute of Aeronautics and Astronautics, 1–7.

Robert, A. J., 1966: The integration of a low order spectral form of the primitive meteorological equations. *J. Meteor. Soc. Japan,* **44,** 237–245.

Roberts, R. D., and J. W. Wilson, 1995: The genesis of three nonsupercell tornadoes observed with dual-Doppler radar. *Mon. Wea. Rev.,* **123,** 3408–3436.

Rotunno, R., J. B. Klemp, and M. L. Weisman, 1988: A theory for strong, long-lived squall lines. *J. Atmos. Sci.,* **45,** 463–485.

Simpson, J., R. Roff, B. R. Morton, K. Labas, G. Dietachmayer, M. McCumber, and R. Penc, 1991: A Great Salt Lake waterspout. *Mon. Wea. Rev.,* **119,** 2241–2270.

Simpson, J. E., 1972: Effects of the lower boundary on the head of a gravity current. *J. Fluid Mech.,* **53,** 759–768.

Smagorinsky, J., 1963: General circulation experiments with the primitive equations: 1. The basic experiment. *Mon. Wea. Rev.,* **91,** 99–164.

Soong, S.-T., 1974: Numerical simulation of warm rain development in an axisymmetric cloud model. *J. Atmos. Sci.,* **31,** 1262–1285.

Wakimoto, R. M., and J. W. Wilson, 1989: Non-supercell tornadoes. *Mon. Wea. Rev.,* **117,** 1113–1140.

——, and B. E. Martner, 1992: Observations of a Colorado tornado. Part II: Combined photogrammetric and Doppler radar analysis. *Mon. Wea. Rev.,* **120,** 552–543.

——, and J. K. Lew, 1993: Observations of a Florida waterspout during CaPE. *Wea. Forecasting,* **8,** 412–423.

——, and N. T. Atkins, 1994: Observations of the sea-breeze front during CaPE. Part I: Single-Doppler, satellite, and cloud photogrammetry analysis. *Mon. Wea. Rev.,* **122,** 1092–1114.

——, and ——, 1996: Observations on the origins of rotation: The Newcastle tornado during VORTEX 94. *Mon. Wea. Rev.,* **124,** 384–407.

Walko, R. L., 1988: Plausibility of substantial dry adiabatic subsidence in a tornado core. *J. Atmos. Sci.,* **45,** 2251–2267.

Wicker, L. J., and R. B. Wilhelmson, 1995: Simulation and analysis of tornado development and decay within a three-dimensional supercell thunderstorm. *J. Atmos. Sci.,* **52,** 2675–2703.

Wilczak, J. M., T. W. Christian, D. E. Wolfe, R. J. Zamora, and B. B. Stankov, 1992: Observations of a Colorado tornado. Part I: Mesoscale environment and tornadogenesis. *Mon. Wea. Rev.,* **120,** 497–520.

Wilhelmson, R. B., and C. S. Chen, 1982: A simulation of the development of successive cells along a cold outflow boundary. *J. Atmos. Sci.,* **39,** 1446–1483.

Wilson, J. W., 1986: Tornadogenesis by nonprecipitation induced wind shear lines. *Mon. Wea. Rev.,* **114,** 270–284.

——, G. B. Foote, N. A. Crook, J. C. Fankhauser, C. G. Wade, J. D. Tuttle, and D. K. Mueller, 1992: The role of boundary-layer convergence zones and horizontal rolls in the initiation of thunderstorms: A case study. *Mon. Wea. Rev.,* **120,** 1785–1815.

Wurman, J., J. M. Straka, and E. N. Rasmussen, 1996: Fine-scale Doppler radar observations of tornadic storms. *Science,* **272,** 1774–1777.

Xu, Q., and M. W. Moncrieff, 1994: Density current circulations in shear flow. *J. Atmos. Sci.,* **51,** 434–446.